

Spectral models for ground motion prediction in the L'Aquila region (central Italy): evidence for stress-drop dependence on magnitude and depth

F. Pacor,¹ D. Spallarossa,² A. Oth,³ L. Luzi,¹ R. Puglia,¹ L. Cantore,⁴ A. Mercuri,⁴ M. D'Amico¹ and D. Bindi⁵

¹ Istituto Nazionale di Geofisica e Vulcanologia, Milan, Italy. E-mail: francesca.pacor@ingv.it

² Dipartimento di Scienze della Terra dell'Ambiente e della Vita, University of Genoa, Italy

³ European Centre for Geodynamics and Seismology, Luxembourg

⁴ Istituto Nazionale di Geofisica e Vulcanologia, Rome, Italy

⁵ Deutsches GeoForschungsZentrum GFZ, Potsdam, Germany

Accepted 2015 October 14. Received 2015 October 13; in original form 2015 May 8

SUMMARY

In this study we derive a spectral model describing the source, propagation and site characteristics of *S* waves recorded in central Italy. To this end, we compile and analyse a high-quality data set composed of more than 9000 acceleration and velocity waveforms in the local magnitude (M_l) range 3.0–5.8 recorded at epicentral distances smaller than 120 km. The data set spans the time period from 2008 January 1 to 2013 May 31, and includes also the 2009 L'Aquila (moment magnitude M_w 6.1, M_l = 5.8) sequence. This data set is suitable for the application of data-driven approaches to derive the empirical functions for source, attenuation and site terms. Therefore, we apply a non-parametric inversion scheme to the acceleration Fourier spectra of the *S* waves of 261 earthquakes recorded at 129 stations. In a second step, with the aim of defining spectral models suitable for the implementation in numerical simulation codes, we represent the obtained non-parametric source and propagation terms by fitting standard parametric models. The frequency-dependent attenuation with distance r shows a complex trend that we parametrize in terms of geometrical spreading, anelastic attenuation and high-frequency decay parameter k . The geometrical spreading term is described by a piecewise linear model with crossover distances at 10 and 70 km: in the first segment, the spectral ordinates decay as $r^{-1.01}$ while in the second as $r^{-1.68}$. Beyond 70 km, the attenuation decreases and the spectral amplitude attenuate as $r^{-0.64}$. The quality factor $Q(f)$ and the high-frequency attenuation parameter k , are $Q(f) = 290f^{0.16}$ and $k = 0.012$ s, respectively, the latter being applied only for frequencies higher than 10 Hz. The source spectra are well described by ω^2 models, from which seismic moment and stress drops of 231 earthquakes are estimated. We calibrate a new regional relationship between seismic moment and local magnitude that improves the existing ones and extends the validity range to 3.0–5.8. We find a significant stress drop increase with seismic moment for events with M_w larger than 3.75, with so-called scaling parameter ε close to 1.5. We also observe that the overall offset of the stress-drop scaling is controlled by earthquake depth. We evaluate the performance of the proposed parametric models through the residual analysis of the Fourier spectra in the frequency range 0.5–25 Hz. The results show that the considered stress-drop scaling with magnitude and depth reduces, on average, the standard deviation by 18 per cent with respect to a constant stress-drop model. The overall quality of fit (standard deviation between 0.20 and 0.27, in the frequency range 1–20 Hz) indicates that the spectral model calibrated in this study can be used to predict ground motion in the L'Aquila region.

Key words: Earthquake ground motions; Earthquake source observations; Seismic attenuation; Site effects.

INTRODUCTION

The Abruzzo region (central Italy) is an area characterized by high seismic hazard, where low to moderate magnitude earthquakes frequently occur (Rovida *et al.* 2011). The most recent seismic sequence started on 2009 April 6 with the extensively studied L'Aquila earthquake (M_w 6.1, M_l 5.8) and lasted for about one year (Chiaraluce *et al.* 2011; Valoroso *et al.* 2013).

In an effort to improve ground motion prediction capabilities in the area, several studies were conducted with the aim of evaluating the different components of the spectral model (i.e. attenuation, source parameters, source scaling and site effects). Different techniques, data sets and/or spatial/temporal windows were adopted in these studies, and while some of them provided a comprehensive set of parameters required for the definition of ground motion, others investigated only specific components. A generalized inversion technique (GIT) was applied by Bindi *et al.* (2009), hereinafter BIN09, to the records of 13 events of the 2009 L'Aquila seismic sequence in order to isolate the source, propagation and site contributions of ground motion. While BIN09 provided rapid insights into the spectral composition of ground motions in the aftermath of the main shock, the data set was however very limited as it was only composed of the waveforms of the main shock and 12 aftershocks with $M_w \geq 4$ at epicentral distances smaller than 200 km. Ameri *et al.* (2011), hereinafter AME11, provided an entire set of spectral terms to predict ground motions after applying the GIT technique to a data set significantly larger than BIN09, containing the records of 100 aftershocks in the local magnitude range $3.1 < M_l < 5.3$ and hypocentral distance range 8–50 km. Malagnini *et al.* (2011), hereinafter MAL11, studied the attenuation of a wide area of the central Apennines using a data set of 170 foreshocks and aftershocks of the L'Aquila sequence ($M_w \geq 2.8$) at distances up to 200 km. Different from the previously mentioned studies, they used a spectral ratio technique to investigate the regional source scaling and employed their attenuation and source scaling results to predict ground motions.

Source scaling was also investigated by Calderoni *et al.* (2013), hereinafter CAL13, through the empirical Green's functions (EGF) approach applied to broad-band signals in the distance range 100–250 km. Both MAL11 and CAL13 found evidence for a stress drop increase for large size earthquakes, contrasting the results of BIN09 and AME11. In particular, CAL13 argued that the contradicting results between their work and BIN09 and AME11 could be partially related to the different methods used to estimate the stress drops and, in particular, to the EGF efficiency in separating source and propagation compared to the GIT.

In order to shed light on these issues and provide the most comprehensive set of spectral parameters for ground motion prediction in the region to-date, we apply the GIT approach to the largest available data set for the area composed of more than 15.000 acceleration and velocity waveforms (about 450 events and 400 stations), recorded in the time span 2008 January 1–2013 May 31 and including the 2009 L'Aquila seismic sequence. This data set provides optimal spatial coverage up to 100 km and reliably spans the magnitude range 3–6.

Following a non-parametric GIT scheme as BIN09 and AME11, we evaluate the complete suite of spectral parameters required for ground motion prediction in a wide region of central Italy. We use parametric models to interpret the non-parametric spectral attenuation curves (in terms of geometrical spreading and anelastic attenuation) and source spectra (in terms of an omega-square model; Brune 1970). The obtained quality factor, stress drops and seismic moments are compared and discussed to the estimates by different

authors for this area. Finally, we reproduce the observed spectral ordinates by performing a forward computation using the parametric models derived in this study and we evaluate their performance through the residual analysis.

DATA SET

The Abruzzo data set is constructed by selecting earthquakes in a geographical area in central Italy constrained by latitude [41 N; 43 N] and longitude [12 E; 15 E]. The bulk of the data originates from the 2009 L'Aquila seismic sequence (Fig. 1). Differently from previous studies (i.e. BIN09, AME11 and MAL11) that analysed subsets of acceleration or velocity data, we exploit all records available from broad-band, short period and accelerometric sensors, belonging to different networks, installed in the area in the time span 2008–2013. The considered networks are: the National Seismic Network, RSN, operated by INGV (Istituto Nazionale di Geofisica e Vulcanologia); the Mediterranean Network, Mednet, operated by INGV; the Rapid Response Networks operated by INGV, RESIF (Reseau Seismologique et Geodesique Francais) and the University of Genoa; the National Accelerometric Network, RAN, operated by the Department of Civil Protection, DPC. We complete the data set by including data from temporary networks deployed for seismic microzonation (Working Group SM-AQ 2010), site effect studies (Bergamaschi *et al.* 2011) and aftershock monitoring (Margheriti *et al.* 2011). Details on instruments and stations of each network are listed in Table 1.

The final data set consists of more than 15.000 records from about 450 events recorded at about 400 stations, in the time period 2008 January 1–2013 May 31 (Fig. 1). The local magnitude range spans from 2.5 to 5.8 and the epicentral distances range up to a maximum of 150 km. The majority of the events were generated by normal faults in the upper crust (i.e. hypocentral depth <15 km).

We carry out an accurate data selection and processing through the following steps:

- (i) Visual inspection of waveforms, instrumental correction and manual picks of P - and S -wave onset; this procedure allows us to identify clipped signals and other specific problems such as signal distortion, spikes, lack of data on the coda, etc.
- (ii) Earthquake location using Hypocentre (Lahr 1989).
- (iii) M_l estimation (Wood–Anderson equivalent).
- (iv) Bandpass filtering: for velocimetric data, we use a fixed frequency band (0.1–40 Hz); for accelerometric data, we adopt the processing procedure of the Italian strong-motion database ITACA (Pacor *et al.* 2011; Paolucci *et al.* 2011).
- (v) Identification of unreliable recordings by comparing the geometric mean of peak ground acceleration (PGA) and velocity (PGV) with the predictions from a ground motion attenuation relation valid for the Italian territory (Bindi *et al.* 2011b): if the difference between predicted and observed strong-motion parameters exceeds 1.5 log units, the waveforms are not further considered.

The local magnitudes are re-computed from synthetic Wood–Anderson seismograms using a local magnitude scale calibrated for the central Italy (M. Cattaneo, personal communication, 2012), in order to have a consistent estimate of the magnitude size for all events. Since the earthquake focal depth is a key parameter for the analysis and interpretation of the inversion results, we put a great deal of effort toward obtaining reliable estimates of this parameter through manual interpretation of the seismograms recorded by temporary networks deployed in the epicentral area. Earthquakes are

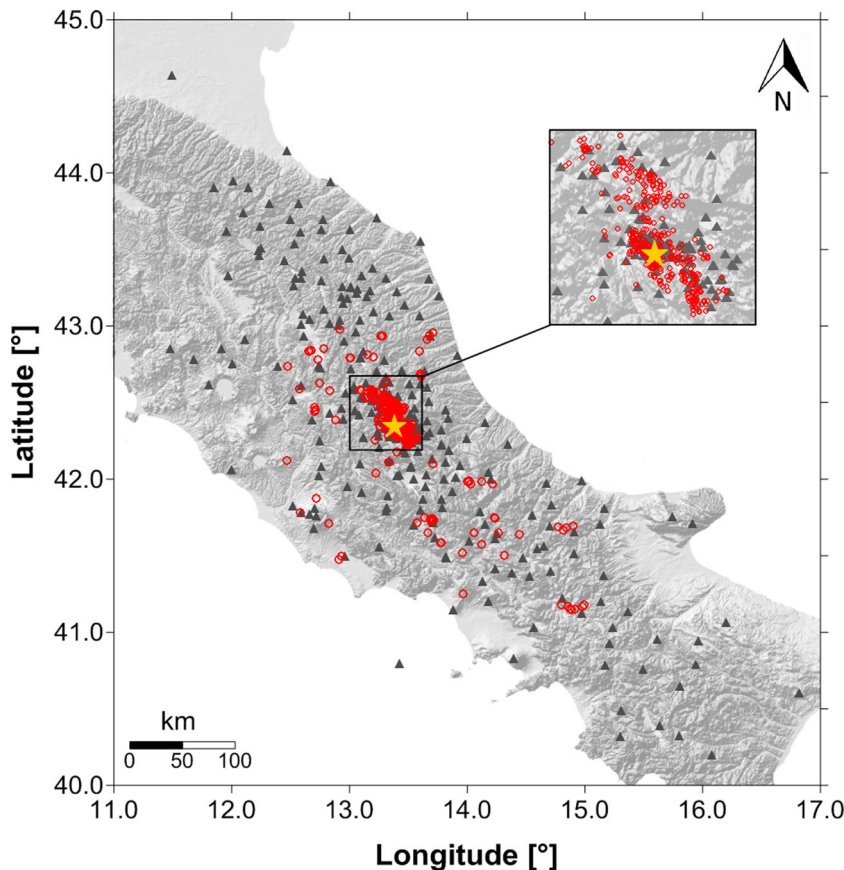


Figure 1. Locations of seismic events (red circles) and recording stations (triangles) considered in this study; the inset highlights the 2009 L'Aquila seismic sequence. The star is the epicentre of the M_w 6.1 main shock.

located using the 1-D propagation model derived by Valoroso *et al.* (2013).

For the selected recordings, we compute Fourier amplitude spectra (FAS) using a distance-dependent energy criterion to determine *S*-wave time window and applying a frequency-dependent threshold to the signal-to-noise ratio (SNR) to select the spectral amplitudes for the inversion. FAS are calculated on time windows starting 0.1 s before the *S*-wave onset and ending when different percentages of the total energy are reached, in function of the source-to-site distance R : (i) 90 per cent when $R < 25$ km; (ii) 80 per cent when $25 \text{ km} < R < 50$ km; (iii) 70 per cent when $R > 50$ km.

As time windows of records close to the epicentre could be very short (< 2 s), we impose a minimum length of 4 s in order to guarantee an acceptable spectral resolution above 1 Hz for the shortest windows. The extracted signals are tapered with Hanning windows with variable length, depending on the selected *S*-waves portion. The spectral amplitudes are calculated considering 90 frequencies, equally spaced in the logarithmic scale, in the range 0.2–40 Hz and smoothed using the Konno & Ohmachi (1998) algorithm, fixing the smoothing parameter b to 40.

Pre-event noise windows of the same length as the signal windows are used to compute the SNRs. Fig. 2 shows examples of waveforms in acceleration for three stations equipped with different sensors and located at different hypocentral distances. The FAS of the selected *S*-wave window and the pre-event noise window are also shown. A frequency-dependent SNR threshold is applied to select the Fourier amplitudes: SNR = 10 at low frequencies (0.2–0.4 Hz), SNR = 5 in the frequency range 0.4–15 Hz and SNR = 10 at frequencies larger than 15 Hz. The large threshold at low frequen-

cies is applied in order to remove FAS related to small-magnitude events that could lead to unreliable estimates of the source spectra. Following this procedure, for each recording the selection of the spectral amplitudes is performed frequency-by-frequency allowing to remove only those portion of the spectra which are dominated by noise (e.g. by microseisms signal in the low-frequency range or by high-frequency anthropic noise).

Selection of the analysed subset

From the whole compiled data set, we extract a data subset applying the following criteria:

- (i) Hypocentral depths shallower than 20 km and local magnitudes in the range 3–5.8 (the latter refers to the magnitude of the main shock of the L'Aquila sequence).
- (ii) Hypocentral distances in the range 1–120 km, since most of the records are related to small-magnitude events and the data coverage for distances larger than 120 km is not complete.
- (iii) Removing stations closer than 1 km, to avoid unbalanced distributions of regional paths.
- (iv) Fourier spectra having at least 50 per cent of points that satisfy the SNR criteria defined above.
- (v) Events recorded by a minimum of 5 stations and stations having at least 10 records.

The selected data set is composed of 261 events and 129 stations (Fig. 3a). Due to the frequency-dependent SNR threshold used to extract the spectral ordinates and the variable window lengths, the number of available spectral amplitudes varies with frequency,

Table 1. Codes, EC8-site classes, latitude, longitude, number of records, networks and installed sensors for the stations used in the inversion.

Code	EC8	LAT	LON	Number of records				Network	Sensor	Number of records			
				Code	EC8	LAT	LON			Network	Sensor		
AMT	B*	42.632	13.286	11	IT-DPC	HN	LG07	B*	42.596	13.662	53	FR-T	HH
ANT	A*	42.418	13.079	24	MZ-Aquila	EH	LG08	B*	42.381	13.662	61	FR-T	HH
AOI	B*	43.55	13.602	41	IV-INGV	HH	LG09	B*	42.448	13.819	14	FR-T	HH
AQ12	B*	42.33	13.378	11	MZ-Aquila	EH	LG10	B*	42.507	13.67	62	FR-T	HH
AQA	B	42.375	13.339	26	IT-DPC	HN	LG11	B*	42.121	13.336	37	FR-T	HH
AQF	B*	42.381	13.355	23	IT-DPC	HN	LG12	D*	42.079	13.514	74	FR-T	HH
AQG	B	42.374	13.337	40	IT-DPC	HN	LG13	A*	42.028	13.65	72	FR-T	HH
AQK	B	42.345	13.401	50	IT-DPC	HN	LG14	B*	42	13.799	69	FR-T	HH
AQM	B*	42.379	13.349	19	IT-DPC	HN	LG15	D*	42.113	13.814	69	FR-T	HH
AQP	A	42.384	13.369	18	IT-DPC	HN	LG16	A*	42.219	13.783	74	FR-T	HH
AQT1	B*	42.774	13.293	10	IV-INGV	EH	LG17	A*	42.319	13.777	74	FR-T	HH
AQU	C*	42.354	13.405	183	IT-DPC	HN	LG18	B*	42.13	13.702	60	FR-T	HH
AQV	B	42.377	13.344	28	IT-DPC	HN	LG19	B*	42.308	13.241	56	FR-T	HH
ARVD	A*	43.498	12.941	39	IV-INGV	HH	LG20	A*	42.205	13.255	37	FR-T	HH
ASSB	A*	43.043	12.659	124	IV-INGV	HH	LNSS	B*	42.603	13.04	154	IV-INGV	HH
AVZ	C	42.028	13.426	21	IT-DPC	HN	LPEL	A*	42.047	14.183	152	IV-INGV	HH
BRS	A*	42.324	13.59	27	IT-DPC	HN	LSS	A*	42.558	12.969	15	IT-DPC	HN
BSSO	A*	41.546	14.594	18	IV-INGV	HH,HN	MGAB	A*	42.913	12.112	56	IT-DPC	HH,HN
BZZ	B	42.337	13.469	24	IT-DPC	HN	MIDA	A*	41.642	14.254	107	IV-INGV	HH,HN
CAF'R	B*	42.227	14.347	68	IV-INGV	HH,HN	MNS	C*	42.386	12.681	165	IV-INGV	HH,HN
CAMP	B*	42.536	13.409	207	IV-INGV	HH	MODR	B*	41.146	13.878	13	IV-INGV	HH
CERA	A*	41.598	14.018	74	IV-INGV	HH,HN	MTCE	A*	42.023	12.742	147	IV-INGV	HH
CERT	A*	41.949	12.982	220	IV-INGV	HH	MTR	B*	42.524	13.245	32	IT-DPC	HN
CESI	D*	43.005	12.905	198	IV-INGV	HH	MURB	B*	43.263	12.525	71	IV-INGV	HH,HN
CESX	A*	42.609	12.587	110	IV-INGV	HH	NOR	C*	42.792	13.092	19	IT-DPC	HN
CHT	B*	42.37	14.148	15	IT-DPC	HN	NRCA	B*	42.833	13.114	175	IV-INGV	HH,HZ
CIGN	B*	41.654	14.905	13	IV-INGV	HH	OFFI	B*	42.935	13.686	180	IV-INGV	HH
CING	B*	43.375	13.195	149	IV-INGV	HH,HN	ORC	B*	41.954	13.642	32	IT-DPC	HN
CLN	B*	42.085	13.521	10	IT-DPC	HN	PCB	B*	42.557	13.336	15	IT-DPC	HN
FAGN	B*	42.266	13.584	187	IV-INGV	HH	POFI	A*	41.717	13.712	144	IV-INGV	HH,HN
FDMO	B*	43.036	13.087	135	IV-INGV	HH	PTQR	A*	42.022	13.401	18	IV-INGV	HH
FEMA	B*	42.962	13.05	19	IV-INGV	HN	PTRJ	A*	41.364	14.529	15	IV-INGV	HH
FIAM	A*	42.268	13.117	220	IV-INGV	HH,HN	RDP	C*	41.758	12.717	15	IV-INGV	HH
FMG	A*	42.268	13.117	18	IT-DPC	HN	RM01	A*	42.277	13.335	151	IV-INGV-T	EH,HN
FRES	B*	41.973	14.669	13	IV-INGV	HH	RM02	B*	42.343	13.328	75	IV-INGV-T	EH,HN
GIUL	A*	41.558	13.255	85	IV-INGV	HH	RM03	A*	42.274	13.472	115	IV-INGV-T	EH,HN
GSA	B	42.421	13.519	43	IT-DPC	HN	RM04	B*	42.188	13.451	89	IV-INGV-T	EH,HN
GUAR	A*	41.794	13.312	133	IV-INGV	HH	RM05	B*	42.439	13.259	163	IV-INGV-T	EH,HN
GUMA	B*	43.063	13.335	169	IV-INGV	HH,HN	RM06	B*	42.377	13.244	123	IV-INGV-T	EH,HN
INTR	A*	42.012	13.905	207	IV-INGV	HH,HN	RM07	B*	42.405	13.406	154	IV-INGV-T	EH,HN
LG01	B*	42.622	13.282	58	FR-T	HH	RM08	B*	42.372	13.505	130	IV-INGV-T	EH,HN
LG02	B*	42.665	13.308	76	FR-T	HH	RM09	B*	42.436	13.186	139	IV-INGV-T	EH,HN
LG03	D*	42.457	13.356	63	FR-T	HH	RM10	B*	42.509	13.186	130	IV-INGV-T	EH,HN
LG04	B*	42.71	13.448	26	FR-T	HH	RM11	B*	42.538	13.277	106	IV-INGV-T	EH,HN
LG05	B*	42.701	13.635	62	FR-T	HH	RM12	A*	42.262	13.392	24	IV-INGV-T	HH
LG06	B*	42.621	13.507	71	FR-T	HH	RM13	B*	42.182	13.581	136	IV-INGV-T	EH,HN
RM14	B*	42.345	13.572	113	IV-INGV-T	EH,HN	SGG	A*	41.387	14.379	11	IV-INGV	HH
RM15	B*	42.282	13.245	25	IV-INGV-T	HH	SMA1	B*	42.631	13.335	34	IV-INGV	EH
RM16	D*	42.235	13.532	66	IV-INGV-T	HH	SNTG	A*	43.255	12.941	28	IV-INGV	HH,HN
RM18	B*	42.55	13.532	59	IV-INGV-T	EH,HN	SSFR	A*	43.436	12.782	13	IV-INGV	HH,HN
RM20	B*	42.525	13.126	71	IV-INGV-T	EH,HN	TERO	B*	42.623	13.604	222	IV-INGV	HH,HN
RM21	B*	42.628	13.142	98	IV-INGV-T	EH,HN	TOLF	B*	42.064	12	18	IV-INGV	HH,HN
RM22	B*	42.444	13.049	70	IV-INGV-T	EH,HN	TRIV	B*	41.767	14.55	22	IV-INGV	HH,HN
RM23	D*	42.58	13.032	69	IV-INGV-T	EH	TRTR	B*	42.808	13.914	46	IV-INGV	HH,HN
RM24	A*	42.171	13.472	58	IV-INGV-T	EH,HN	VAGA	A*	41.415	14.234	30	IV-INGV	HH,HN
RM25	B*	42.622	13.281	16	IV-INGV-T	EH,HN	VCEL	A*	42.395	13.841	215	IV-INGV	EH
RM26	B*	42.457	13.356	24	IV-INGV-T	EH,HN	VVLD	B*	41.87	13.623	175	IV-INGV	HH
RM27	A*	42.302	13.68	19	IV-INGV-T	EH,HN	X101	B*	42.331	13.303	28	IV-INGV-T	HN
RM28	B*	42.402	13.549	25	IV-INGV-T	EH,HN	X102	B*	42.397	13.314	21	IV-INGV-T	HN
RM29	B*	42.561	13.202	10	IV-INGV-T	EH,HN	X104	B*	42.36	13.338	96	IV-INGV-T	EH,HN
RMP	C*	41.811	12.702	38	IV-INGV	HH	X105	D*	42.311	13.463	33	IV-INGV-T	HN
RNI2	A*	41.703	14.152	94	IV-INGV	HH,HN	X106	A*	42.307	13.384	48	IV-INGV-T	EH,HN
SACR	A*	41.397	14.706	11	IV-INGV	HH,HN	X107	B*	42.473	13.248	37	IV-INGV-T	HN
SACS	B*	42.849	11.91	21	IV-INGV	HH,HN	X110	A*	42.226	13.779	15	IV-INGV-T	HN
SDM	A*	42.29	13.558	11	IT-DPC	HN							

*Indicates that the soil category is assigned on the base of geological information.

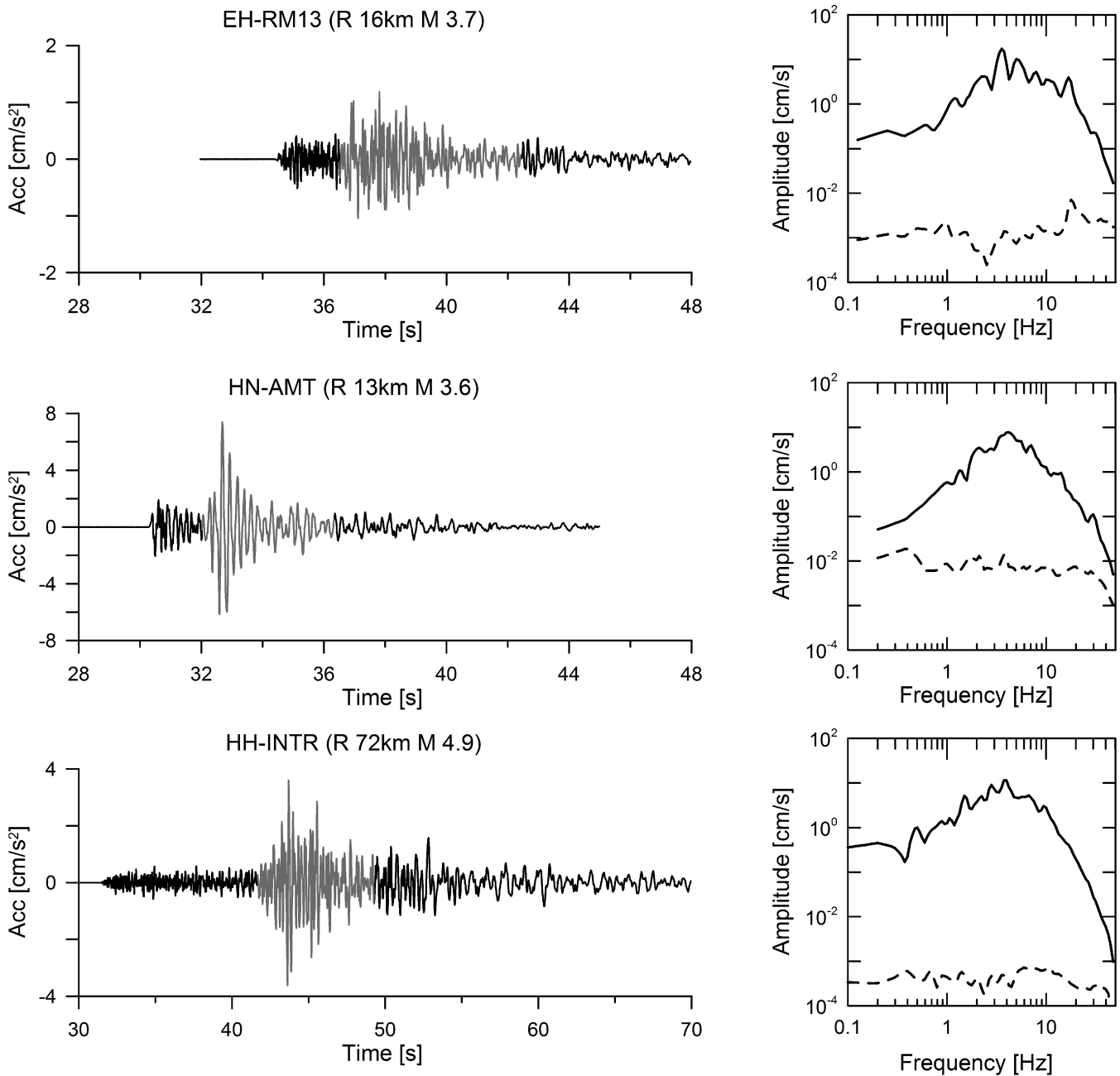


Figure 2. Left: Time histories converted in acceleration from a short period—EH (top), strong motion—HN (middle) and broad-band—HH (bottom) sensors; the selected S-wave window is indicated in grey and for each record; the sensor code, the station code, the hypocentral distance and magnitude are reported. Right: Fourier amplitude spectra computed for the S-wave window (continuous line) and the pre-event noise window (dashed line).

decreasing from about 9250 in the frequency range 1–10 Hz to about one-third for lower and higher frequencies. To preserve a good data redundancy for the least-squares inversion and considering the limit on the spectral resolution imposed by the window lengths, we select the frequency range 0.4–25 Hz for the following analysis. The number of available spectral amplitudes is 7160 and 5200 at 0.4 and 25 Hz, respectively.

According to geological information, most of the recording stations can be classified as rock (EC8-A class), stiff soil (EC8-B class) or soft soil (EC8-C) sites (Table 1). Site amplification effects are relevant for the L'Aquila data set (e.g. Bergamaschi *et al.* 2011; Puglia *et al.* 2011; Di Giulio *et al.* 2014), since the epicentral area is located inside a river valley filled with quaternary deposits

of various depths. Geological conditions are so variable that over a distance of few tens of metres the shear wave velocities of the shallower soil layers may differ substantially, as shown by the soil profiles available for some strong-motion stations from the Italian accelerometric archive (ITACA, <http://itaca.mi.ing.it>; Luzi *et al.* 2008; Pacor *et al.* 2011).

The selected data set provides an optimal spatial coverage up to 100 km, in the magnitude range 3–5, as shown by the map of the path rays (Fig. 3b) and magnitude–distance distribution (Fig. 4a). Fig. 4(b) shows the distribution of the records as a function of magnitude, hypocentral distance, depth and FAS window duration. The bulk of the data are from small-magnitude events ($M_1 < 4$) and hypocentral distances in the range 5–80 km. Magnitudes larger

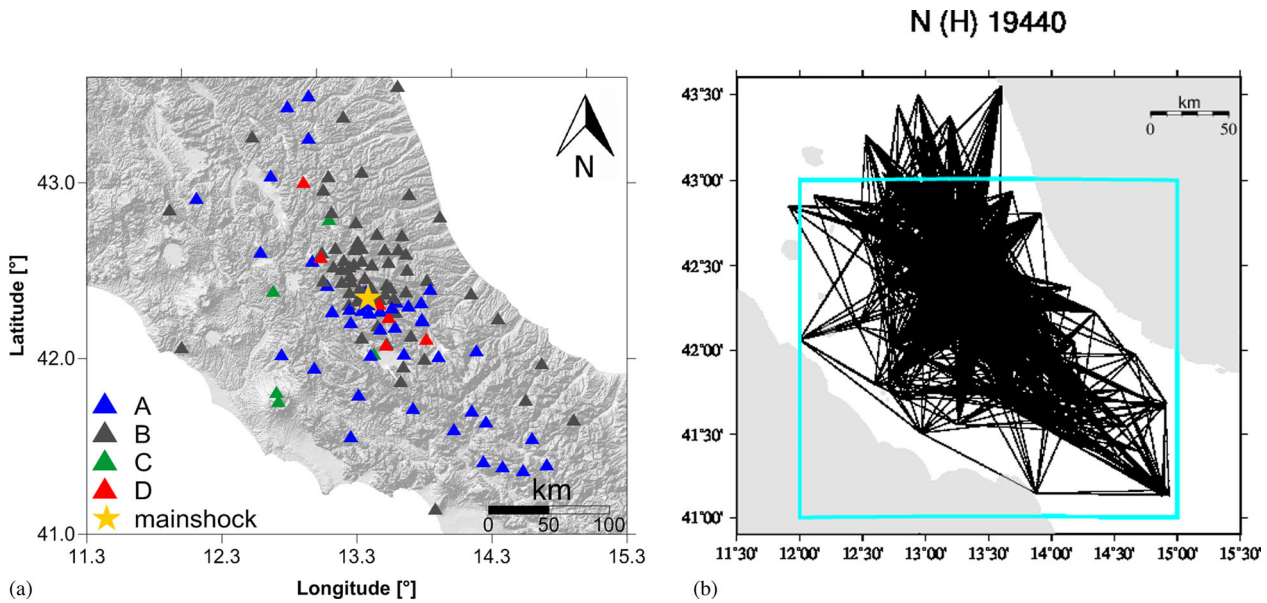


Figure 3. (a) Locations of selected recording stations, colour coded according to the EC8 site classes. (b) Map of seismic-ray paths at $f = 5.9$ Hz; the blue square represents the area where the selected earthquakes are located.

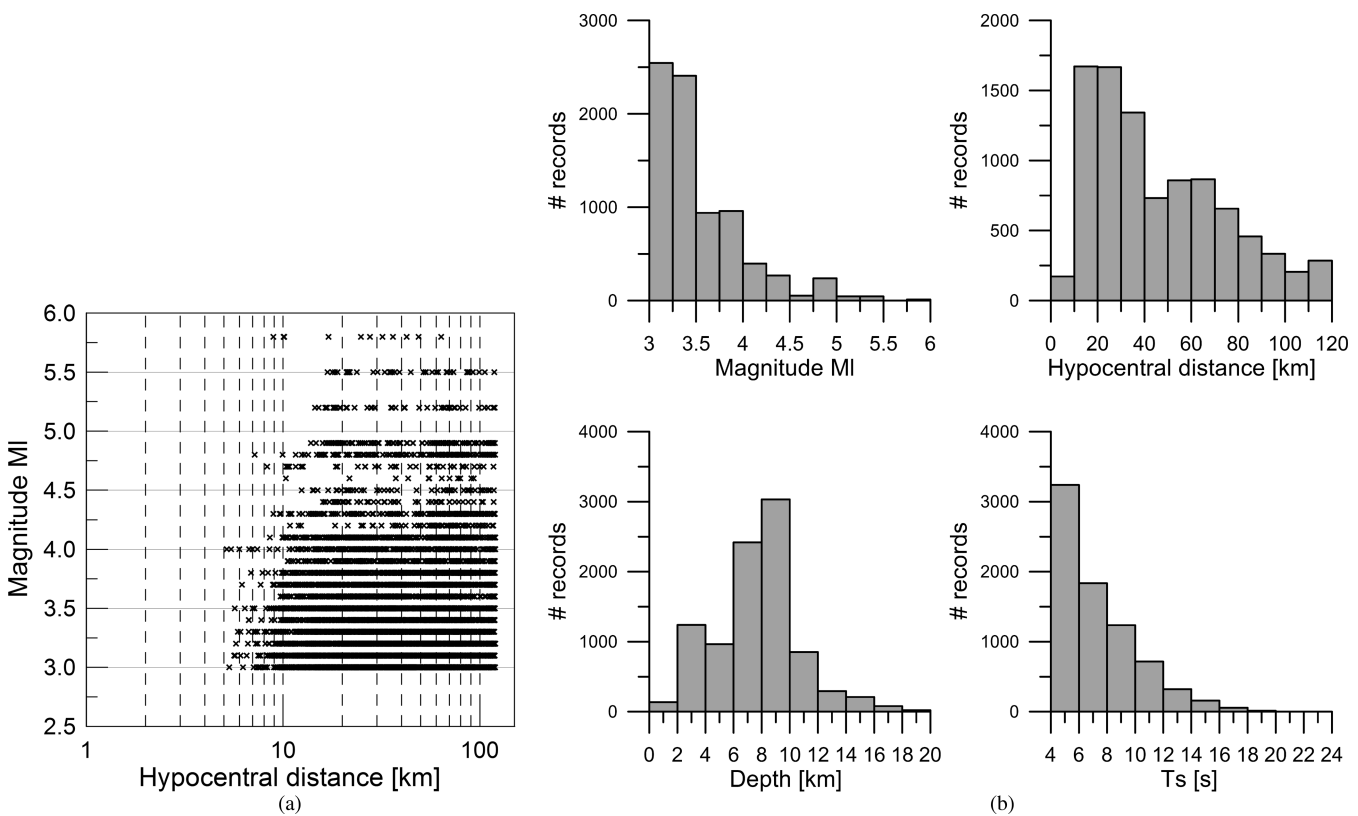


Figure 4. (a) Magnitude-distance distribution of the selected data set at frequency $f = 5.9$ Hz. (b) Histograms of local magnitudes, hypocentral distances, hypocentral depths and S-wave durations of the considered recordings.

than 5 relate to the three largest events of the L'Aquila sequence. Most recordings originate from events located at depths larger than 6 km. The S-wave windows are generally short (< 10 s) since the waveforms were mostly recorded close to the epicentres on rock and stiff soil sites. The selected window lengths range between 4 s and 19.5 s, with median of 6 s (Fig. 4b).

In Fig. 5, the acceleration spectral amplitudes at 0.4 and 5.9 Hz are plotted versus magnitude and hypocentral distance. Besides the expected attenuation with distance and amplitude increase with magnitude, Fig. 5 shows clear frequency-dependent attenuation rates and dispersion of the spectral values, both increasing with frequency. To isolate in these trends the source, propagation and site

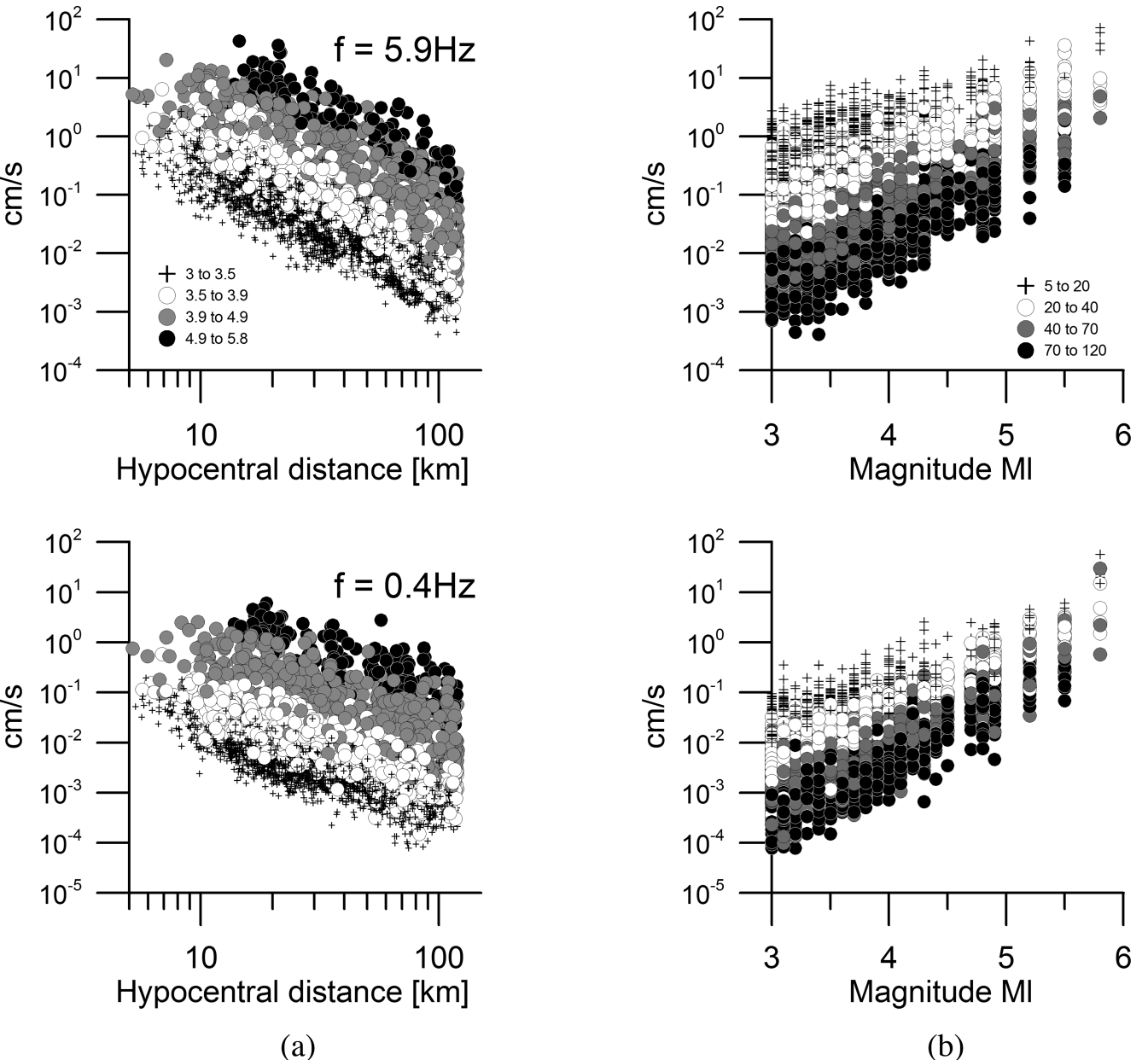


Figure 5. (a) Acceleration spectral amplitudes at 5.9 Hz (top) and 0.4 Hz (bottom), as a function of hypocentral distance (the symbols indicate different magnitude ranges). (b) Acceleration spectral amplitudes at 5.9 Hz (top) and 0.4 Hz (bottom), as a function of magnitude (the symbols indicate different hypocentral distance ranges).

contributions, we apply a non-parametric inversion scheme as described in the following section.

METHOD

The GIT is a well-known method to isolate frequency-dependent attenuation characteristics, source spectra and site response functions (Andrews 1986; Castro *et al.* 1990).

The acceleration spectral amplitude of ground motion can be written as:

$$\log_{10} U_{ij}(f, M_i, r_{ij}) = \log_{10} S_i(f, M_i) + \log_{10} A(f, r_{ij}) + \log_{10} G_j(f) \quad (1)$$

where $U_{ij}(f, M_i, r_{ij})$ represents the amplitude of the FAS at the j th station resulting from the i th earthquake with magnitude M_i ; r_{ij} is the hypocentral distance; $S_i(f, M_i)$ is the source spectrum of the i th earthquake, $A(f, r_{ij})$ is the attenuation operator and $G_j(f)$ is the site response function of the j th station.

The solution of the system described by eq. (1) can be performed either following a parametric approach, where the unknown functions related to source and propagation are expressed in terms of standard models (e.g. Kawase 2006; Tsuda *et al.* 2006, 2010; Salazar *et al.* 2007; Drouet *et al.* 2008, 2011), or following a non-parametric inversion scheme (e.g. Castro *et al.* 1990; Parolai *et al.* 2000, 2004; Oth *et al.* 2008, 2009). In this study, given the good data coverage available, we follow a non-parametric inversion scheme that allows us to capture possible modulations of the attenuation with distance (e.g. effects of later arrivals) and to highlight deviations

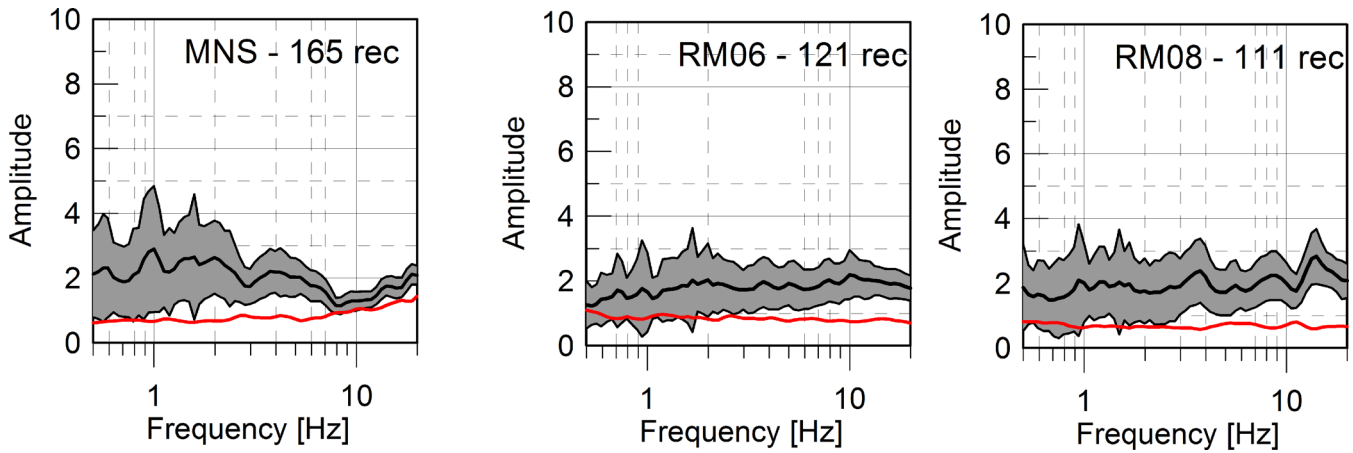


Figure 6. Comparison between the horizontal to vertical (H/V) spectral ratio (black and grey area indicate mean and the \pm one standard deviation, respectively) and the vertical amplification function obtained by GIT (red curve) for the three selected reference stations (MNS, RM06 and RM08); the number *rec* of *S*-phases available for each station is also provided.

from standard source models. The inversion is performed in a single step (Oth *et al.* 2011), for the vector composition of the horizontal components, H , considering 73 frequencies from 0.4 to 25 Hz, equally spaced in logarithmic scale. The hypocentral distance range from 1 to 120 km is discretized into 60 bins, each 2 km wide. The system is solved in a least-squares sense (Paige & Saunders 1982) and 200 bootstrap replications are performed at each frequency for evaluating the uncertainties (Efron 1979).

In order to remove two unresolved degree of freedom affecting eq. (1), two constraints have to be added. The attenuation is applied from a reference distance of 5 km (i.e. $A(f, 5) = 1$ for any frequency) and, consequently, the source spectra are shifted to the same reference distance. Moreover, to eliminate the linear dependence between the source and site terms, the site amplification function for one or more reference stations is constrained to one. For the selection of the reference stations, we perform a preliminary inversion for the vertical component, setting the average response of all sites to 1, and we also compute the horizontal to vertical spectral ratio (H/V) for all stations. The reference stations were then selected with the following criteria: (i) amplifications smaller than 2 on vertical component of the site response function resulting from GIT; (ii) flat horizontal-to-vertical spectral ratio H/V , or characterized by small-amplitude peaks (<2.5). Three stations were finally selected as reference sites (RM06, RM08 and MNS) and Fig. 6 shows the H/V and vertical component amplification results for these stations.

Before discussing the results of the non-parametric inversion, we analyse the goodness of fit of the non-parametric models by computing the residual distributions, shown in Fig. 7. The residuals, computed as the observed minus predicted spectral values, do not show any trend with magnitude and distance, and they have almost zero mean with standard deviations of about 0.2 for all considered distance and magnitude bins. We conclude that the performed non-parametric inversion provides empirical functions that well describe the overall trends present in the data.

RESULTS

Attenuation functions

Fig. 8(a) shows the non-parametric attenuation functions at different frequencies as a function of the hypocentral distance. The attenuation functions show a clear dependence on frequency and,

generally, they decrease monotonically with distance up to 100 km, with a rate increasing with frequency. A rapid decay is observed, for all frequencies up to about 70 km.

In order to obtain those parameters useful for ground motion predictions and simulation (Boore 1983), we fit the non-parametric attenuation functions with a model including the geometrical spreading and the frequency-dependent attenuation term in the form:

$$A(f, r_{ij}) = G(r) \exp \left[\frac{-\pi f(r - r_0)}{Q(f) v_s} \right] \exp [-\pi k f] \quad (2)$$

where $G(r)$ is the geometrical spreading attenuation, v_s is the shear wave velocity, r_0 is the reference distance, Q is the apparent quality factor, assumed frequency-dependent and k is parameter describing the high-frequency attenuation, as proposed by Anderson & Hough (1984).

It is known that the estimates of the geometrical spreading and the quality factor are inherently difficult to obtain and are affected by errors that cannot be solved without a clear understanding on the attenuation mechanisms in the propagation medium (Mitchell 2010). These uncertainties arise because, while the empirical curves are the results of complex phenomena that occur in the earth crust, the models used to fit them are generally very simple. The main problem in reproducing the attenuation curves by eq. (2) is the existing trade-off between geometrical spreading and frequency-dependent quality factor Q (Xie 2010; Atkinson 2012; Babaie Mahani & Atkinson 2012; Castro *et al.* 2013; McNamara *et al.* 2014).

To face this problem, different inversion strategies can be implemented: (i) to fix the geometrical spreading exponent n for specific distance range and evaluate the frequency dependence of Q (Castro *et al.* 2013; McNamara *et al.* 2014); (ii) to assume geometrical spreading variable with distance and frequency while Q is assumed constant and independent on frequency (Morozov 2010); (iii) to consider both n and Q depending on frequencies (Bindi *et al.* 2004). Independently on the adopted inversion scheme, without other external constraints, the trade-off between the quality factor and geometrical spreading remains in any case unresolved.

In this study, we follow a two-step approach: in the first step, we determine the frequency-independent geometrical spreading model $G(r)$ while, in the second, we consider the data corrected for $G(r)$ to derive the frequency-dependent attenuation model that includes the quality factor Q and the high-frequency decay parameter k .

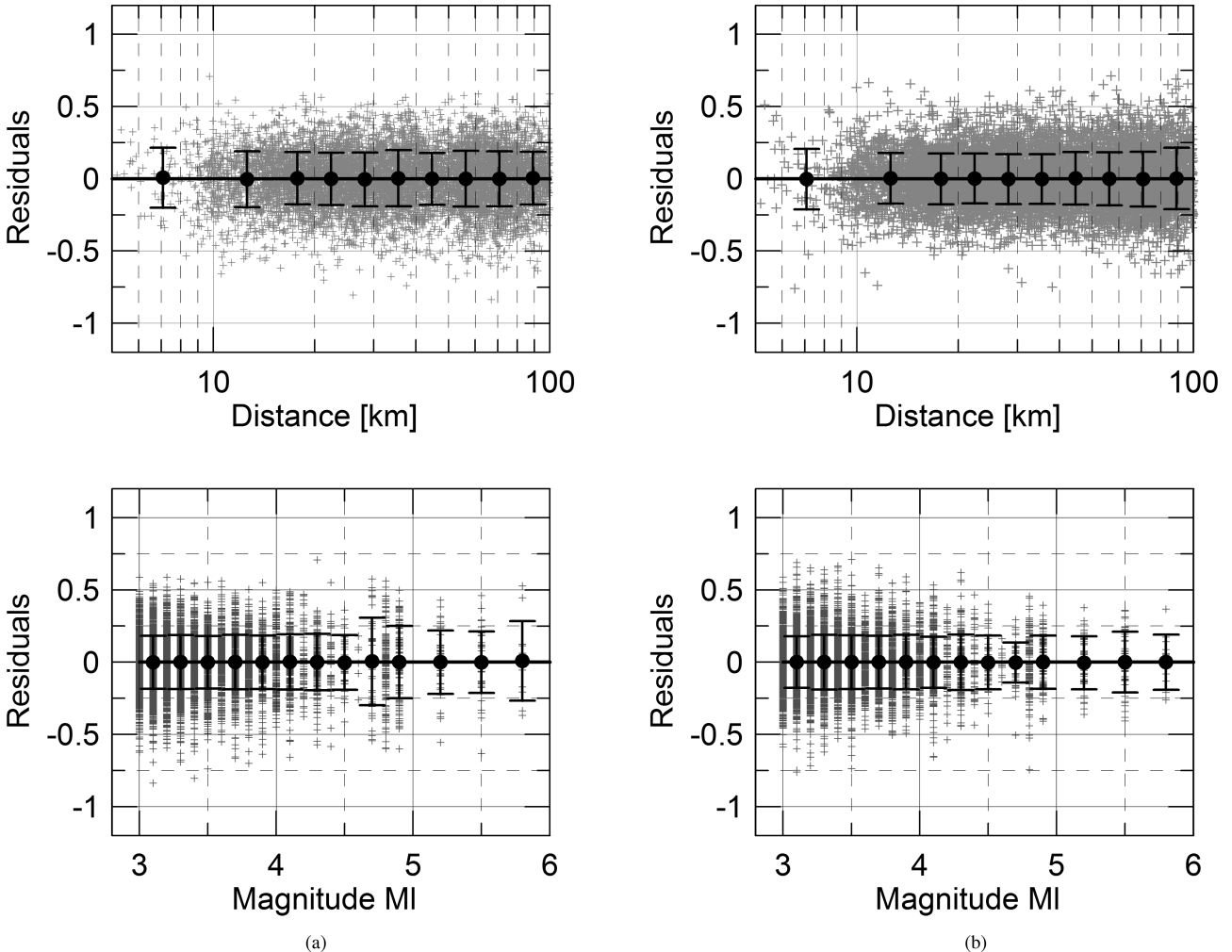


Figure 7. Residuals (grey symbols), computed as \log_{10} (observation/prediction), at 1 Hz (a) and 10 Hz (b) as a function of distance (top) and magnitude (bottom); the mean residuals \pm one standard deviation computed for different distance and magnitude bins are shown as black dots with error bars.

To minimize the effect of the anelastic attenuation, we perform the first regression by selecting the non-parametric curves around 1 Hz (i.e. from 0.8 to 1.2 Hz) and considering a tri-linear hinged model with crossover distances at 10 and 70 km, in the following form:

$$G(r) = \begin{cases} \left(\frac{r_0}{r}\right)^{n_1}, & \text{for } r \leq 10 \text{ km} \\ \left(\frac{r_0}{10}\right)^{n_1} \left(\frac{10}{r}\right)^{n_2}, & \text{for } r > 10 \text{ km and } r \leq 70 \text{ km} \\ \left(\frac{r_0}{10}\right)^{n_1} \left(\frac{10}{70}\right)^{n_2} \left(\frac{70}{r}\right)^{n_3}, & \text{for } r > 70 \text{ km} \end{cases} \quad (3)$$

The hinge distances are selected on visual inspection of the empirical curves in Figs 8(a) and (b) and performing preliminary trial-and-error regressions to minimize the residuals. The best least-squares solution corresponds to $[n_1; n_2; n_3] = [1.08; 1.64; 0.64]$, as shown in Fig. 8(b) together with the empirical data. This model predicts strong attenuation up to 70 km; beyond this distance the decay rate decreases, since the signals are dominated by reflected and refracted waves that attenuate slower. AME11 already suggested a distance decay in epicentral area described as r^{-3} and interpreted either as an effect of S waves travelling through the fault zone of the L'Aquila main shock, or to the geometrical spreading of the near-field terms.

As discussed in Yenier & Atkinson (2015), a geometrical spreading faster than r^{-1} at short and intermediate distances is not an

uncommon feature, considering that the real propagation medium is far from to be homogenous. A strong geometrical spreading at short and intermediate distances is observed in other worldwide regions, such as Western North America (Atkinson 2004; Babaie Mahani & Atkinson 2012) and Central and Eastern America (Yenier & Atkinson 2015). Numerical simulations in a typical layered medium also indicate that the distance decay in the epicentral area can be described by geometrical spreading with exponent greater than 1 (Frankel 1991; Chapman & Godbee 2012).

The entire set of non-parametric curves corrected for the geometrical spreading given in eq. (3) are used to find the attenuation parameters $Q(f) = Q_o f^\alpha$ and k , fitting the following model:

$$AK(f) = \begin{cases} \exp\left(\frac{-\pi f(r-r_0)}{\beta Q_0 f^\alpha}\right) \exp(-\pi k(f-10)), & \text{for } f \geq 10 \text{ Hz} \\ \exp\left(\frac{-\pi f(r-r_0)}{\beta Q_0 f^\alpha}\right), & \text{otherwise} \end{cases} \quad (4)$$

Taking the logarithm of both sides of eq. (4), we evaluate the Q_0 , α and k values through a least-squares regression in the frequency range 0.4–25 Hz. The obtained best-fit model is given by:

$$Q(f) = (290 \pm 3) f^{(0.16 \pm 0.01)} \text{ and } k = (0.012 \pm 0.001) \quad (5)$$

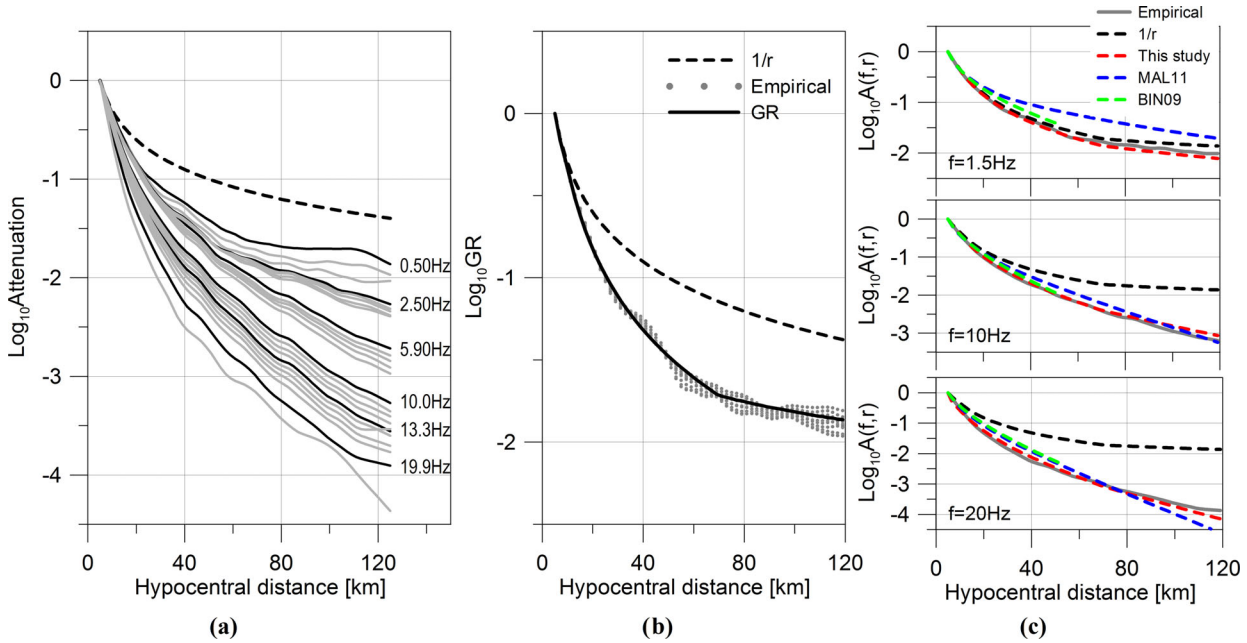


Figure 8. (a) Non-parametric spectral attenuation curves versus distance. Black lines are the attenuation curves at selected frequencies. The dashed black line indicates r^{-1} decay. (b) Geometrical spreading (black curve) fitting the empirical attenuation values (grey dots) in the frequency range 0.8–1.2 Hz. (c) Total attenuation models, composed by geometrical spreading and frequency-dependent attenuation term, plotted versus hypocentral distances at 1.5 Hz (top), 10 Hz (middle) and 20 Hz (bottom). The colour lines indicate the different models, the black line the r^{-1} decay. The grey lines indicate the non-parametric attenuation curves.

Table 2. Attenuation models for L'Aquila region (AME11: Ameri *et al.* 2011; BIN09: Bindi *et al.* 2009; MAL11: Malagnini *et al.* 2011).

	$Q(f)$	r_0 (km)	Geometrical spreading	Distance range (km)
AME11	$23.28f^{0.58}$	8	$1/r$	6–30
BIN09	$59f^{0.56}$	11	$1/r$	8–50
MAL11	$140f^{0.25}$	40	$\begin{cases} r^{-1.1} & r \leq r_1 = 10 \text{ km} \\ \left(\frac{1}{r_1}\right)^{1.1} \left(\frac{r}{r_1}\right)^{-1.0} & r_1 < r \leq r_2 = 30 \text{ km} \\ \left(\frac{1}{r_1}\right)^{1.1} \left(\frac{r_2}{r_1}\right)^{-1.0} \left(\frac{r}{r_2}\right)^{-0.7} & r > r_2 \end{cases}$	10–200
This study	$290f^{0.16}$	5	$\begin{cases} \left(\frac{r_0}{r}\right)^{1.08} & r \leq r_1 = 10 \text{ km} \\ \left(\frac{r_0}{10}\right)^{1.08} \left(\frac{10}{r}\right)^{1.64} & r_1 \leq r \leq r_2 = 70 \text{ km} \\ \left(\frac{r_0}{10}\right)^{1.08} \left(\frac{10}{70}\right)^{1.64} \left(\frac{70}{r}\right)^{0.64} & r \geq r_2 \end{cases}$	5–120

Due to the trade-off between geometrical spreading and anelastic attenuation, a meaningful comparison of our Q -frequency relations with other studies is only possible when the estimates of Q are made using the same distance attenuation function. For this reason, in Fig. 8(c) and Table 2 we compare the whole attenuation model, that is, composed by geometrical spreading, quality factor and high-frequency terms as inferred in this work, with those from previous studies for L'Aquila region.

Within 50 km from the hypocentre, our model predicts similar attenuation rate to BIN09, although the quality factor and the distance decay are parametrized in different way. In comparison to MAL11, the main differences are observed for low frequencies and at distances larger than 20 km, where our model attenuates faster.

Source spectra

In order to derive the source parameters (i.e. seismic moments and corner frequencies) of the earthquakes in our data set, we fit the non-

parametric acceleration source spectra to the omega-square model (Brune 1970):

$$S(f) = \frac{\Re_{\theta\varphi} FV}{4\pi\rho\beta^3 r_0} M_0 (2\pi f)^2 \frac{1}{1 + \left(\frac{f}{f_c}\right)^2} \quad (6)$$

where $\Re_{\theta\varphi}$ is the average radiation pattern for S waves, in this study set to 0.55; $V = \sqrt{2}$ is the partition of S -wave energy into the two horizontal components; $F = 2$ is the free-surface amplification and $\rho = 2.8 \text{ g cm}^{-3}$ is the density; β is the shear wave velocity; r_0 is the reference distance in kilometres; M_0 denotes the seismic moment and f_c is the corner frequency. For each event, we derive M_0 and f_c through a non-linear regression by applying an iterative least-squares algorithm. M_w is then computed from seismic moment using the relation of Hanks & Kanamori (1979). Finally, the seismic

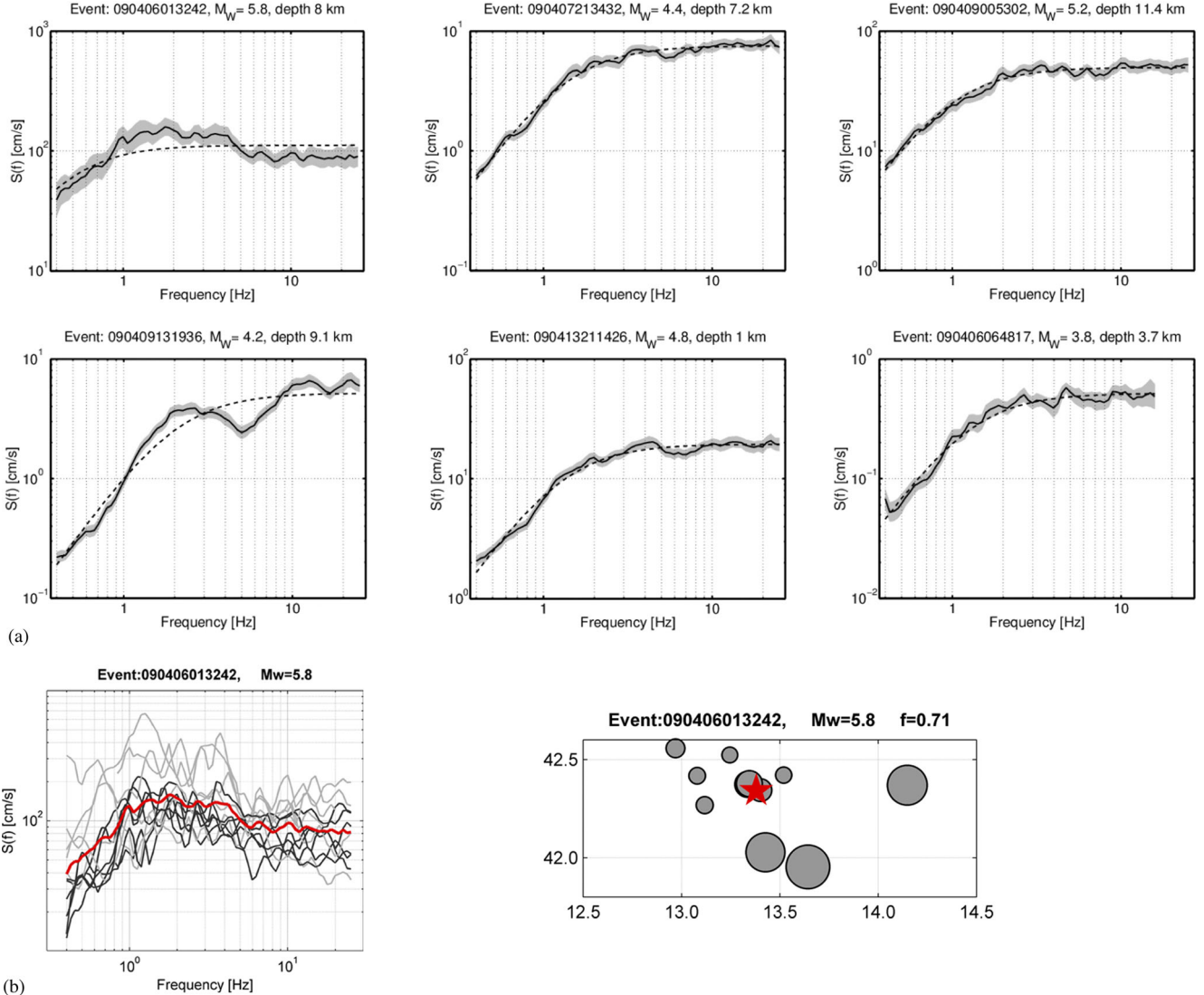


Figure 9. (a) Non-parametric spectral source functions (black lines), with standard deviations, compared to Brune source model (dashed lines). (b) Left: non-parametric source spectrum of 2009 L'Aquila main shock (red curve) and observed spectra corrected for empirical attenuation and site functions (grey and black lines are for stations located south and north to the epicentre, respectively). Right: spatial distribution of the spectral ordinates of right panel corrected for attenuation and site functions at 0.71 Hz. Red star is the epicentre of the 2009 L'Aquila main shock.

moment and the corner frequency are used to determine the stress drop $\Delta\sigma$ using standard relationships (Brune 1970):

$$\Delta\sigma = \frac{7M_0}{16R^3}, \quad (7)$$

where

$$R = \frac{2.34 \cdot \beta}{2\pi f_c} \quad (8)$$

is the source radius.

Seismic moment

The non-parametric source functions obtained from the inversion are shown in Fig. 9 for six events approximately spanning the considered magnitude range. Each spectrum is compared with the corresponding omega-square model showing that the non-parametric spectra can be satisfactorily explained using Brune's source model, with very few exceptions (e.g. event 090409131936 in Fig. 9a). Con-

cerning the main shock of the L'Aquila seismic sequence (event 090406013242), the empirical source function shows a bump in the frequency band 0.5–5 Hz. This shape could be explained by the presence of forward directivity effects at stations located to the southeast of the epicentre (Ameri *et al.* 2012). The observed spectra, corrected for attenuation and site functions inferred from the inversion (Fig. 9b), confirm the asymmetric distributions of spectral amplitudes with the largest values in the southeastern region with respect to the epicentre. CAL 13 and Calderoni *et al.* (2015) identified directivity effects in other events of L'Aquila sequence by applying the spectral ratio technique. However, these directivity effects are not observed in the source spectra as inferred by GIT since the non-parametric curves represent a sort of average source spectra as seen by the network. Since we selected only well-sampled events (i.e. earthquakes recorded by at least 10 stations) and with a good azimuthal coverage, differences in the spectral amplitudes at each single station due to directivity effects are expected to be averaged out, allowing for a robust estimation of the corner frequencies and seismic moment.

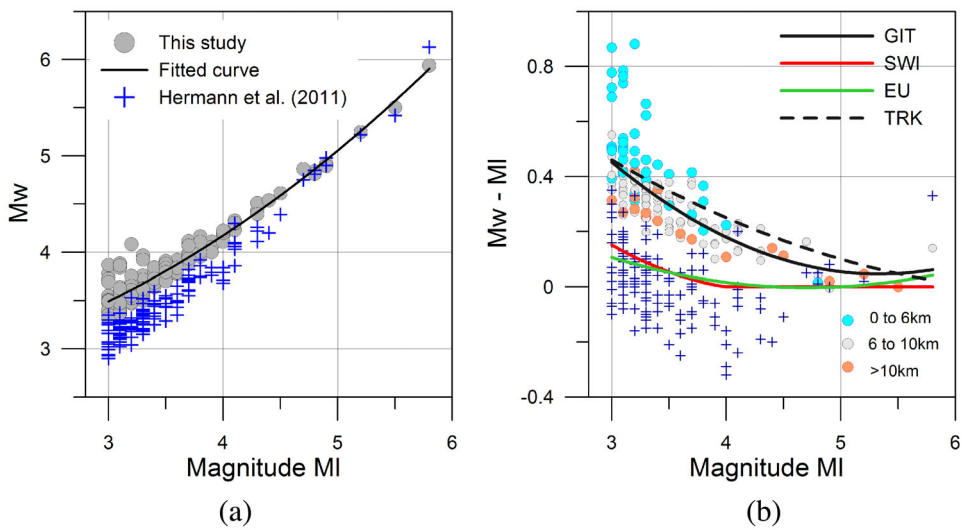


Figure 10. (a) Moment magnitude (M_w) estimated from the inverted source spectra (circles) versus local magnitude (M_l). The black line represents the quadratic model. The blue crosses indicate the M_w values estimated by Herrmann *et al.* (2011). (b) Magnitude difference $M_w - M_l$ versus M_l . The circles are the difference computed considering the M_w from this study, where the colours represent different depth intervals. The blue crosses are the difference computed considering the Herrmann magnitudes. The lines are different relationships between M_w and M_l . Continuous black: the best fit for this study; dashed black: Parolai *et al.* (2007) model shifted by 0.5 magnitude units; green and red lines: Grünthal *et al.* (2009) and Goertz-Allmann *et al.* (2011) relationships, respectively, shifted by 0.3 M_w units.

Following Oth *et al.* (2011), we verify if the empirical source spectra are affected by the effect of the average high-frequency decay k through the fit to the Anderson & Hough (1984) model, for frequencies higher than 10 Hz. The obtained values are normally distributed with an average $k = -0.003 \pm 0.01$ s. This means that the high-frequency decay does not affect the source spectra and is included in the attenuation and the site terms, an observation that has also been made in a range of other studies using this methodology (e.g. Oth & Kaiser 2014).

The computed moment and local magnitudes are used to investigate the $M_w - M_l$ scaling (Fig. 10). A continuous positive curvature is expected when the scaling between M_w and M_l is analysed over a broad magnitude range (Bakun 1984; Hanks & Boore 1984). Therefore, a quadratic term is generally considered to fit the scaling over a broad magnitude range with a single relation (e.g. Ben-Zion & Zhu 2002; Parolai *et al.* 2007; Grünthal *et al.* 2009). Also for the analysed data set, the trend is well described by a quadratic scaling:

$$M_w = 0.074M_l^2 + 0.21M_l + 2.16 \quad (9)$$

and shown in Fig. 10(a). The 95 per cent confidence intervals for the quadratic coefficient (0.074 ± 0.036) confirms its significance.

For common events, the M_w estimates of this study are compared to the moment magnitudes M_w^H computed by Herrmann *et al.* (2011) using a moment tensor analysis (blue crosses in Fig. 10a). For magnitudes smaller than 4.8, the M_w^H is, on average, 0.30 units smaller than the M_w from GIT, while the two moment magnitude estimates agree for larger earthquakes. Differences of the same magnitude order (about 0.22) were also discussed by Scognamiglio *et al.* (2010) and Herrmann *et al.* (2011) comparing their results with the moment magnitudes estimates by Pondrelli *et al.* (2010) using a regional moment tensor analysis.

Fig. 10(b) reports the difference between M_w and M_l versus M_l for this study, compared to the differences obtained from empirical relationships derived for other regions. To this aim, we consider the models derived in a wide M_l range (lower than 1 and up to 5.9) for Switzerland (Goertz-Allmann *et al.* 2011), European continental re-

gions (Grünthal *et al.* 2009) and northwestern Turkey (Parolai *et al.* 2007). Since a systematic vertical offset can appear when different models are compared, even for the same region, due to differences in some model parameters (e.g. velocity model or earthquake locations), in Fig. 10(b) the models from other regions are arbitrarily shifted to make the comparison among the magnitude scaling of the different relations easier.

For $M_l > 4.5$, the $M_w - M_l$ scaling in the L'Aquila region is almost flat (in the M_l range 4.5–6, M_w varies from 4.59 to 6.06), in agreement with the scaling observed for the other regions shown in Fig. 10. For smaller magnitudes, the curvature of the $M_w - M_l$ scaling obtained in this study is significantly stronger than the one observed for Switzerland and central Europe. On the other hand, when compared to the scaling obtained for another seismic sequence occurred in a shallow crustal active region (i.e. the 1999 Izmit earthquake in northwestern Turkey), the two scaling behaviours reasonably agree. Although a more representative statistical sample is needed to draw any definitive conclusions, Fig. 10(b) suggests that regional dependences could affect the $M_w - M_l$ scaling.

Source scaling of the L'Aquila sequence

To investigate the source properties in terms of stress drop, we restrict the analysis to the epicentral area of the sequence and select 231 events in a spatial window with latitude range 42.0–42.8 and longitude range 12.6–13.6.

Stress drops were calculated through eqs (7) and (8), assuming a variation of S-wave velocity with depth. The adopted velocity-depth function is the 1-D model by Bianchi *et al.* (2010), obtained from receiver function analyses and used by Ameri *et al.* (2012) to simulate the recorded ground motions of L'Aquila main shock. The estimated stress drops have a mean equal to 2.6 MPa, with the bulk of the observations ranging between 1 and 5 MPa (Fig. 11a), and can be described by a lognormal distribution with mean 0.25 and standard deviation 0.32 in log units. The stress-drop range is comparable to what was observed for single crustal seismic sequences

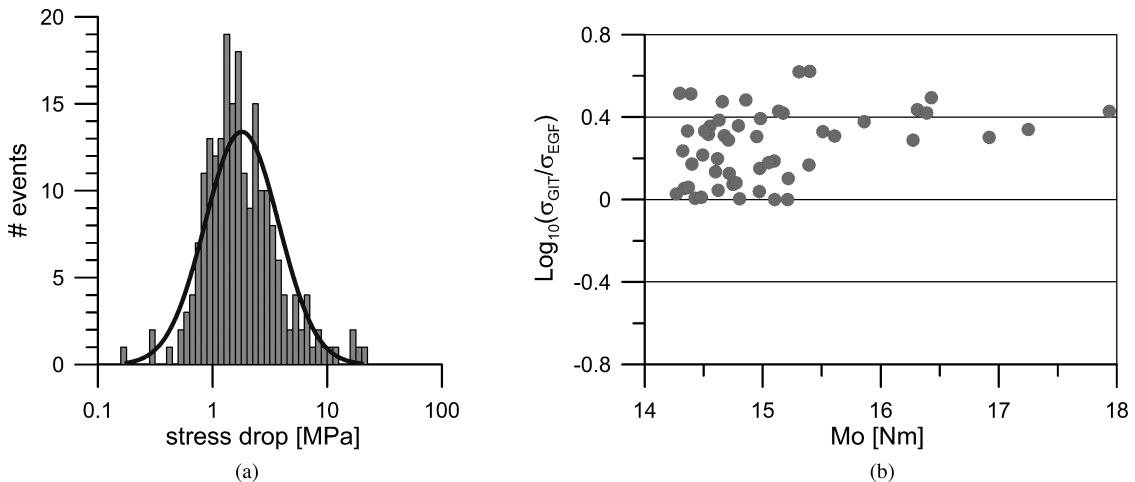


Figure 11. (a) Distribution of stress drops of the events of the L'Aquila sequence and fitted lognormal distribution. (b) Logarithm of the ratio between stress drops from this study and from CAL12 (EGF approach, Calderoni *et al.* 2013) as function of seismic moment.

Table 3. Moment magnitude and stress-drop variability for L'Aquila region (GIT: generalized inversion technique; EGF: empirical Green's function technique).

	M_w	Number of event	$\Delta\sigma$ (MPa)	Method
AME11	3.0–5.3	112	0.3–60.0	GIT
BIN09	4.1–6.3	13	2.4–16.8	GIT
MAL11	2.8–6.1	170	1.0–15.0	EGF
CAL13	3.3–6.1	64	0.5–10.0	EGF
This study	3.3–5.9	231	0.2–25.0	GIT

in other regions of the world, for instance in Japan (Oth 2013) and Canterbury, New Zealand (Oth & Keiser 2014), in contrast with the large scatter observed for global data (Allmann & Shearer 2007), where the stress drops span up to 4 order of magnitude.

The range of our estimates is also in agreement with BIN09, MAL11 and CAL13, while the range of variability of AME11 is the largest (Table 3). We compare the stress drops obtained with the EGF approach (CAL13) with the ones obtained in this study (Fig. 11b) and find a persistent bias, roughly independent on magnitude. The EGF approach is based on single station spectral ratios, and therefore stress drops of events are relative one to the other, as absolute values are obtained fixing the stress drop of a reference event. CAL13 selected the event of 2009 April 7 (12:29, M_w 3.59) as reference. The stress drop of this event is 1.3 MPa (see their Table 2),

approximately half of the value obtained in this study (2.16 MPa). The mean bias (0.26) equals the log of the ratio between the two estimates for the reference event.

Fig. 12 shows the stress-drops plotted versus hypocentral depth and moment magnitude: despite the large scatter, a depth-dependence of the average stress drop can be observed, with increasing average values for depths shallower than 6 km, between 6 and 10 km and deeper than 10 km. A significant increase of stress drop with magnitude is also observed with an average value of 1 MPa at M_w 3 and 10 MPa at M_w 5.8.

Earthquake source scaling has been a persistently controversial issue over the past decades. Aki (1967) was the first to hypothesize the self-similarity of earthquakes, implying that the stress drop is constant independent of earthquake size. Large data sets from different seismotectonic regions usually do not show a breakdown in self-similarity (e.g. Shearer *et al.* 2006; Allmann & Shearer 2007; Oth *et al.* 2010), yet studies on single seismic sequences often provide indications that smaller events have lower stress drops than larger ones (e.g. Mayeda & Malagnini 2010; Mereu *et al.* 2013; Malagnini *et al.* 2014). For the Colfiorito (1997–1998) and L'Aquila (2009) seismic sequences, Malagnini *et al.* (2008, 2011) found a clear departure from self-similarity, given by stress drops around 22 MPa for the largest events (M_w 6.0) and around 5 MPa for smaller magnitudes (e.g. M_w 4.0). Similarly, CAL13 recognized an increasing

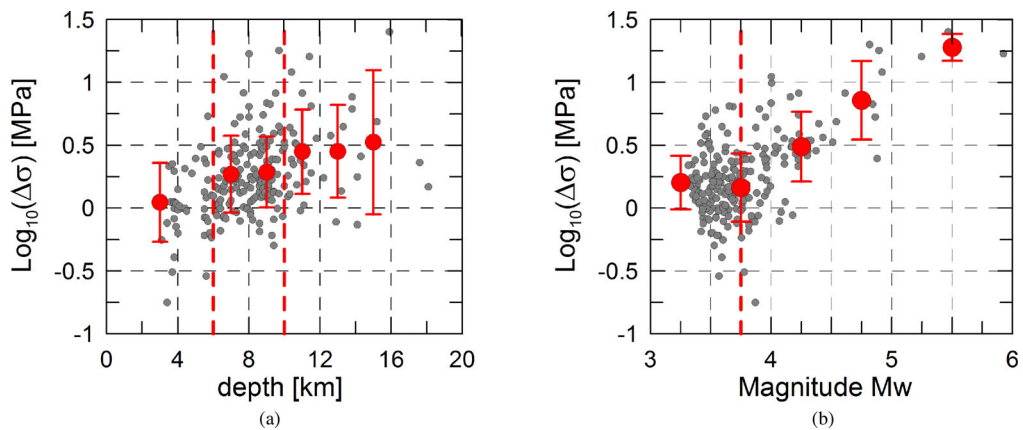


Figure 12. (a) Stress drops versus hypocentral depths and (b) stress drops versus moment magnitude. Red circles and lines indicate mean residuals and standard deviations, for different depths and magnitude bins. The vertical dashed lines indicate the hinge depth and magnitude used for the analysis (see eq. 9).

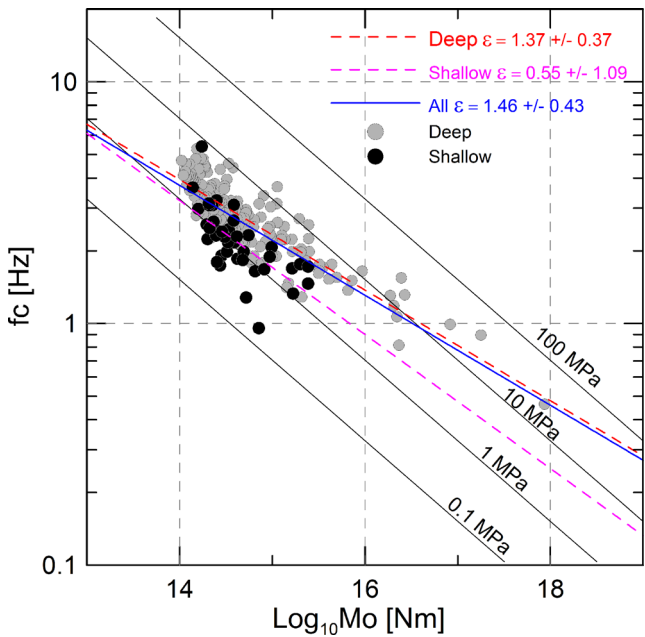


Figure 13. Corner frequency scaling versus seismic moment. Grey lines represent constant stress-drop relationships. Grey crosses indicate shallow events with depth $H \leq 6$ km, while black dots indicate deep events with $H > 6$ km. Models for the corner frequency scaling in terms of ε parameter are also shown, considering the whole data set (blue dashed line), only the shallow (pink dashed) and only deep (orange dashed) earthquakes.

trend for stress drop from smaller events (1 MPa at M_w 3.3) to larger events (10 MPa at M_w 6.1) of the L'Aquila sequence. Our results confirm a correlation between stress drop and moment magnitude (Fig. 12). Following Kanamori & Rivera (2004), we estimate the deviation from self-similarity through the ε parameter, such that $M_0 \propto f_C^{-(3+\varepsilon)}$. According to this parametrization ε equals 0 in case of self-similarity, $\varepsilon > 0$ indicates increasing stress drop with earthquake size and $\varepsilon < 0$ indicates the opposite trend (e.g. Oth & Kaiser 2014).

Fig. 13 shows the set of seismic moments and corner frequencies estimated for the 231 events of the L'Aquila sequence. A linear regression has been performed on the $\log f_C$ versus $\log M_0$ data points in order to estimate ε and 100 bootstrap replications have been calculated in order to estimate the 95 per cent confidence intervals. ε is close to 1.5 with an uncertainty of about 0.5 when considering the entire data set, in agreement with the significant stress drop increase seen in Fig. 12. When we distinguish between shallow ($H < 6$ km) and deep events ($H \geq 6$ km), the latter continue to show a dependence on magnitude, while no definitive conclusion can be given for shallow events, due to the large uncertainty associated to the ε and in view of the narrow available magnitude range for the shallow events.

Stress-drop models

We investigate the source scaling using two models for the stress-drop dependency on seismic moment. In the first model (Model A), the stress drop is assumed to be linearly dependent on the seismic moment, that is:

$$\log_{10} \Delta\sigma = a + b \log_{10} M_0, \quad (10)$$

where a and b are the regression coefficients.

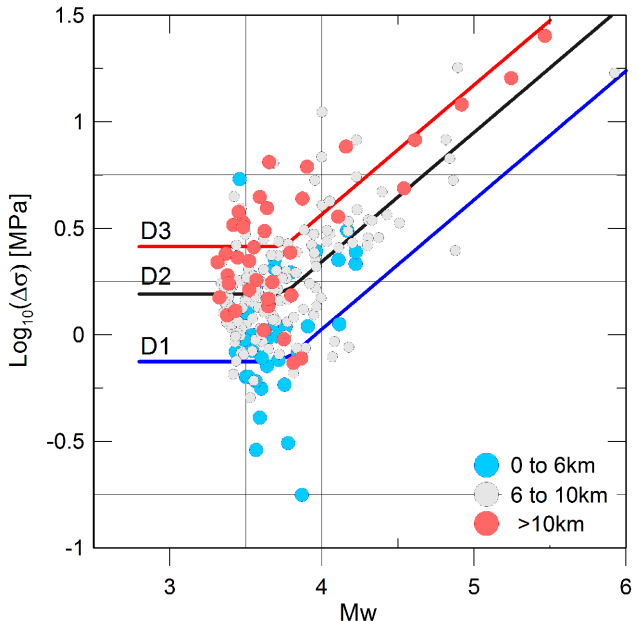


Figure 14. Stress-drop scaling with seismic moment. Continuous lines represent model B described by eqs (11) and (12). Blue circles indicate events with depths $H \leq 6$ km, grey circles events with depths in the range 6–10 km; red circles events with $H > 10$ km. The piecewise linear functions represent the model for the three depth ranges ($D1$, $D2$ and $D3$) considering the systematic deviations as provided by the depth-dependent random effects (see text for details).

Table 4. Coefficients for stress-drop models (H is the hypocentral depth).

	Model A (eq. 10)	Model B (eqs 11 and 12)
a	-4.484	0.159
b	0.322	0.404
δ_k (random effects on the parameter a)		$\delta_{D1} = 0.254$ for $0 \leq H < 6$ km $\delta_{D2} = 0.031$ for $6 \leq H < 10$ km $\delta_{D3} = -0.285$ for $H \geq 10$ km
Standard deviation	0.259	0.227

In order to account for the features observed in Fig. 12, we test also a model including both the stress-drop dependence on depth and its dependence on seismic moment through a piecewise linear function on logarithmic scales. We follow a mixed effect approach (e.g. Pinheiro & Bates 2000), where the depth is categorized into three intervals, indicated with $k = D1, D2, D3$ and introduced in the model as random effect over the offset parameter in the form

$$\log_{10} \Delta\sigma = f(M) + \delta_k + \varepsilon. \quad (11)$$

where

$$f(M) = \begin{cases} a & \text{for } M_0 < M_0^{\text{ref}} \\ a + b \log_{10}(M_0/M_0^{\text{ref}}) & \text{otherwise} \end{cases} \quad (12)$$

In eq. (12), a (offset) and b (slope) are the fixed-parameter of the model, M_0^{ref} is the hinge seismic moment used to define the piecewise linear function (i.e. a constant stress-drop model below the hinge magnitude and a linear increasing model above the hinge magnitude). In eq. (11), δ_k are the random effects on the offset parameter a and ε is the residual distribution. The random effects depend on three *a-priori* selected depth categories $D1, D2, D3$. After testing several combinations of depth categories and threshold magnitude, we adopt a regression model (Model B) defined by a hinge seismic moment corresponding to $M_w = 3.75$ and by the

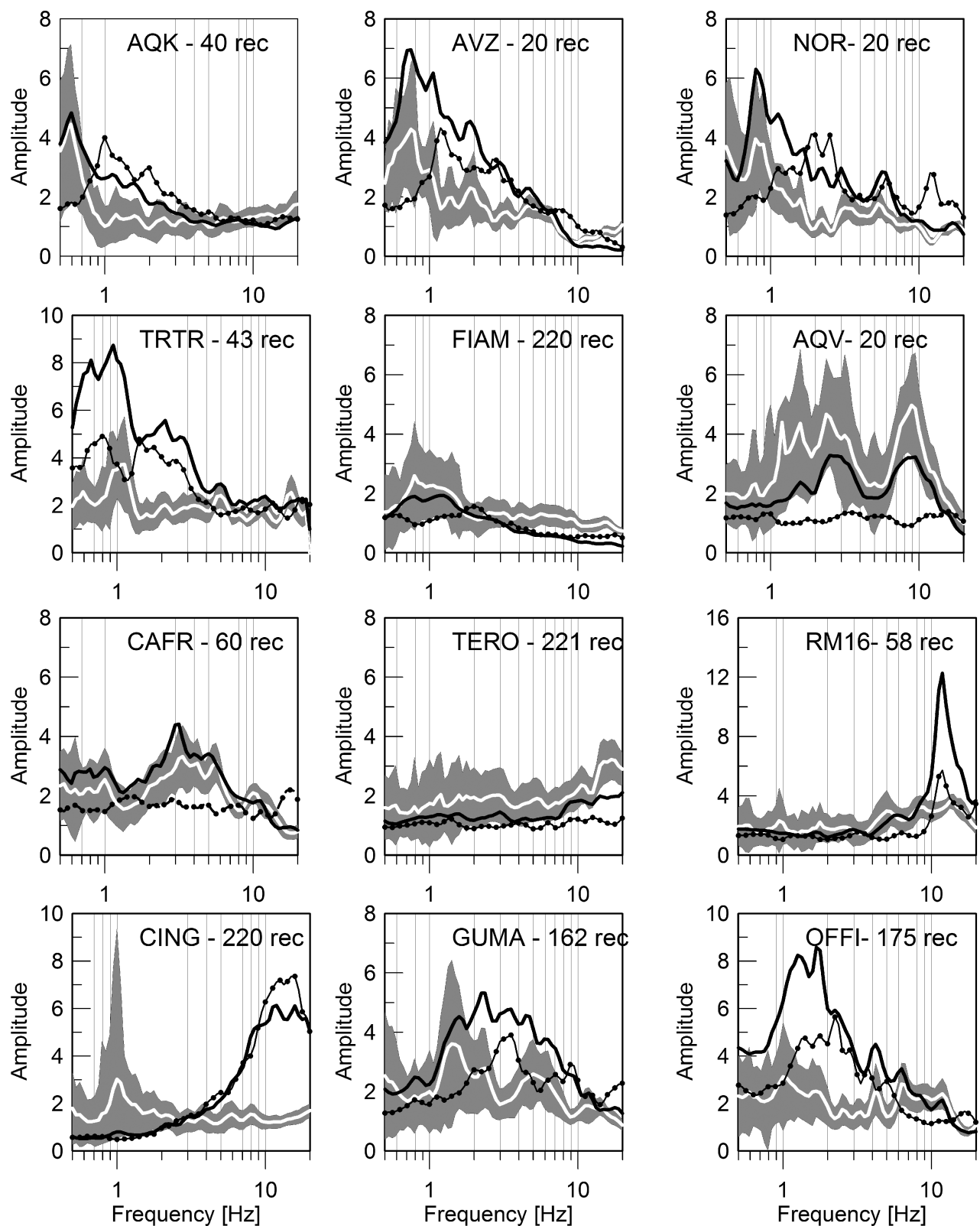


Figure 15. Site amplification functions for 12 selected sites. Empirical site amplifications obtained from the GIT for horizontal (black thick line) and vertical (black dotted lines) components and from H/V ratio (white lines) are plotted. The grey shaded areas indicate the mean and the standard deviations of the H/V from earthquakes recordings. The number of records for each station is also reported.

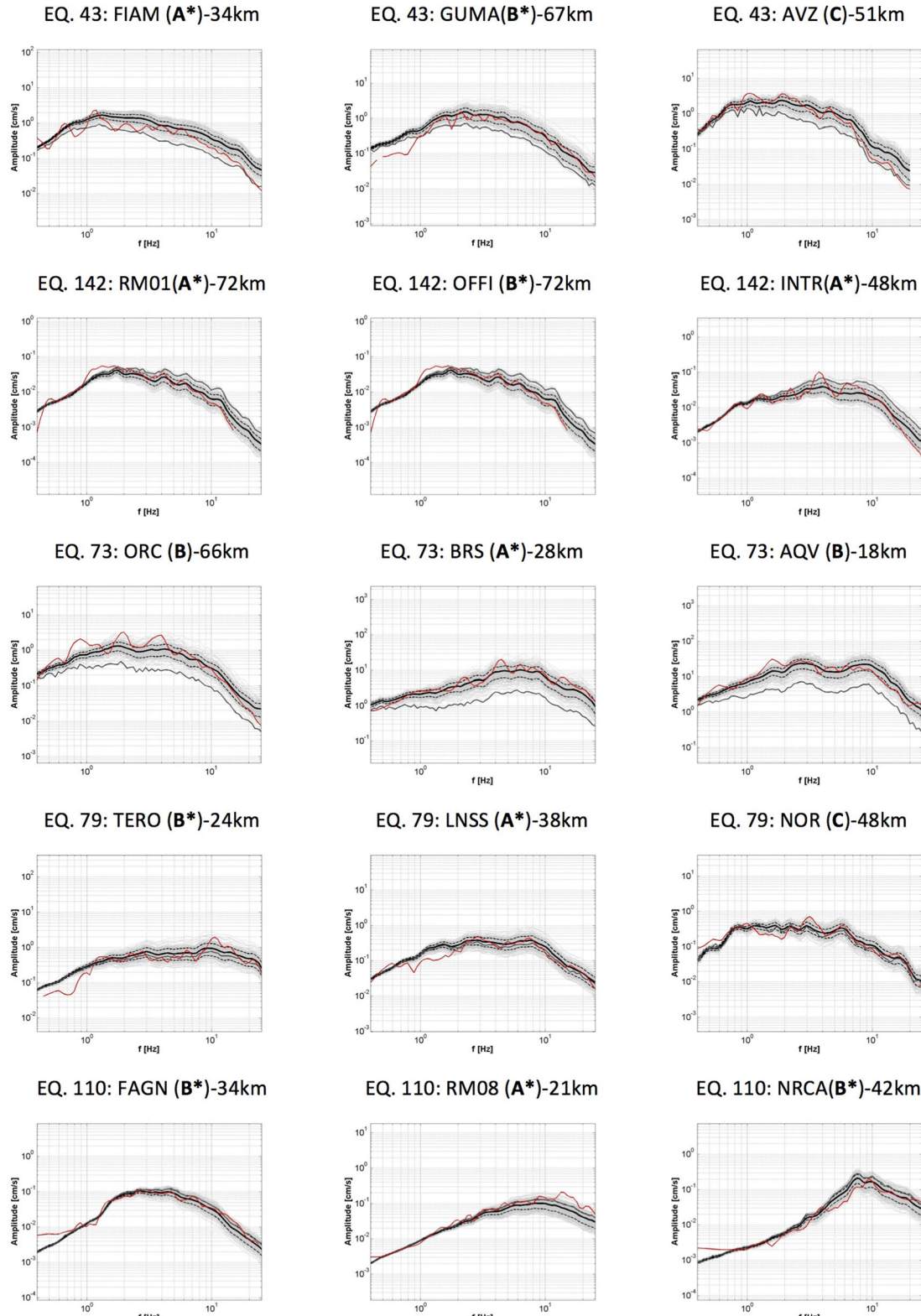


Figure 16. Comparison of observed and simulated Fourier spectra (FAS) for 5 events (see Table 5) and 15 sites. Red curve: observed spectra (geometrical mean of horizontal components). Thin grey lines: theoretical FAS computed with eq. (11) and the Monte Carlo method. Thick black and dashed lines: mean \pm standard deviation of theoretical spectra. Thick grey line indicates theoretical FAS computed assuming constant stress drop (2.6 MPa).

Table 5. Events used for comparison between theoretical and observed Fourier spectra.

Number of events	date yyyyymmddhhmmss	#rec	H (km)	M_w	Mo (Nm)	$\Delta\sigma$ (MPa)
43	20090406231539	44	10.4	4.9	2.7E+16	5.9
142	20090425020826	57	4	3.6	3.34E+14	0.7
73	20090409005302	44	11.4	5.2	8.3E+16	8.4
79	20090409043247	53	7.2	4.4	4.4E+15	3.5
110	20090412163556	50	6.6	3.3	1.4E+14	1.6

following three depth categories: $D1 = [0\text{--}6]$, $D2 = [6\text{--}10]$, $D3 \geq 10$ km. Inversion results for Model B reported in Fig. 14 shows that the depth grouping has a clear effect on the offset a . The regression results and the standard deviation of Models A and B are listed in Table 4. The introduction of the random effect depending on the hypocentral depth improves the fit of the regression, reducing the standard deviation of the residuals by about 10 per cent. The results indicate that the source scaling for the L'Aquila region can be described by a model which includes a stress-drop dependence on seismic moment for magnitude larger than 3.75, with an overall offset controlled by the hypocentral depth.

Site functions

Examples of site response functions that result from the non-parametric inversion are displayed in Fig. 15, whereas the entire set of amplification functions is reported in the Electronic supplement. When independent estimates were available from other studies, we also verified the consistency of the results. This is the case of stations AQV and AQK (Puglia *et al.* 2011) and NOR (Bindi *et al.* 2011a), for which the amplification levels and the fundamental frequencies are in agreement with the results from standard spectral ratios.

The site functions are also compared with H/V ratios computed directly from the FAS used in the non-parametric inversion. On average, when no amplification on the vertical component occurs, the two estimates agree in term of shapes (e.g. FIAM, AQV, CAFR, TERO). On the other hand, when the vertical ground motion is amplified, the two curves can significantly differ and the H/V curves cannot be used as estimators of the site response.

Examples are stations AVZ, NOR, AQK and TRTR for amplification of the vertical at low-frequency, GUMA and OFFI for amplification at intermediate frequency, RM16 and CING for vertical amplification at high frequency. As already observed by other authors (Ameri *et al.* 2011; Bergamaschi *et al.* 2011), the empirical functions found in this study confirm the large variability of the site response in the Abruzzo region that cannot be taken into account using simple site-classification based on geological information (Table 1). Furthermore, this study also confirms the relevance of the amplification on the vertical motions, indicating that in the L'Aquila region, the H/V ratio should be used with caution for evaluating the local site response.

SPECTRAL PARAMETERS FOR GROUND MOTION PREDICTION

The reliability of the spectral models used to parametrize attenuation $A(f, r)$ and the source spectra $S(f)$, including the stress-drop models, are tested by simulating the observed acceleration spectra for L'Aquila data set in the distance range 5–120 km. The empirical amplification functions obtained by the inversion are assumed as the response of soil sites.

The source spectra are modeled by an omega-square model with seismic moments estimated from the inversion and stress drop given by the empirical relationship in eq. (11). The frequency-dependent attenuation with distance is described by the global attenuation model of eq. (2), where the geometrical spreading is as in eq. (4). The quality factor $Q(f)$ and the high-frequency decay parameter k are given in eq. (5).

In order to take into account the uncertainties associated with the model parameters, we assume quality factor and stress drop as drawn from respective lognormal distributions. The empirical amplification functions are also represented as lognormal distribution, with mean and standard deviation obtained from the bootstrap analysis applied in the non-parametric inversion. Based on these distributions, the theoretical FAS of each site-source couple is evaluated through 500 Monte Carlo simulations.

Fig. 16 shows the comparison between the geometric mean of theoretical and observed spectra for the horizontal components at several stations for the events listed in Table 5 (in the moment magnitude range 3.5–5.2 and hypocentral depths 4–12 km). We consider stations characterized by different site responses, such as stations located on rock (FIAM, LNSS, TERO and the reference site RM08), stations showing amplification over a broad frequency band (ORC, INTR), or affected by strong site effects at high (NCRA, BRS), intermediate (GUMA, AQV, FAGN) or low (NOR, AVZ, OFFI) frequencies. In Fig. 16, the theoretical FAS computed using a fixed stress drop (2.6 MPa) are also reported. In general, the simulated spectra (black curves) using an increasing stress drop with magnitude and depth fit the observations reasonably well, especially in case of the strongest events, where the improvement of using variable stress drop is more evident (e.g. earthquakes 73 and 43 in Table 5).

To evaluate the reliability of the proposed spectral models, we compute the residuals between the observed data and the simulated spectral amplitudes. The residuals distributions at 1 and 10 Hz are shown in Figs 17 and 18 for variable and constant stress-drop models, respectively. The fitted Gaussian distributions show a mean distribution around 0 with standard deviations slightly increasing with frequency, varying from 0.2 and 0.27 (Table 6). The residuals computed using a constant stress drop show a clear dependence on magnitude, confirming that a stress-drop magnitude scaling is necessary to better fit the observed data. These results indicate that the proposed source, site and attenuation models are suitable to describe the seismic motion recorded in the L'Aquila region.

CONCLUSIONS

We analysed a data set composed of more than 9000 acceleration or velocity seismic records selected in the Abruzzo region in the time period 2008 January 1–2013 May 31, covering the local magnitude range 3.0–5.8 and epicentral distances shorter than 120 km.

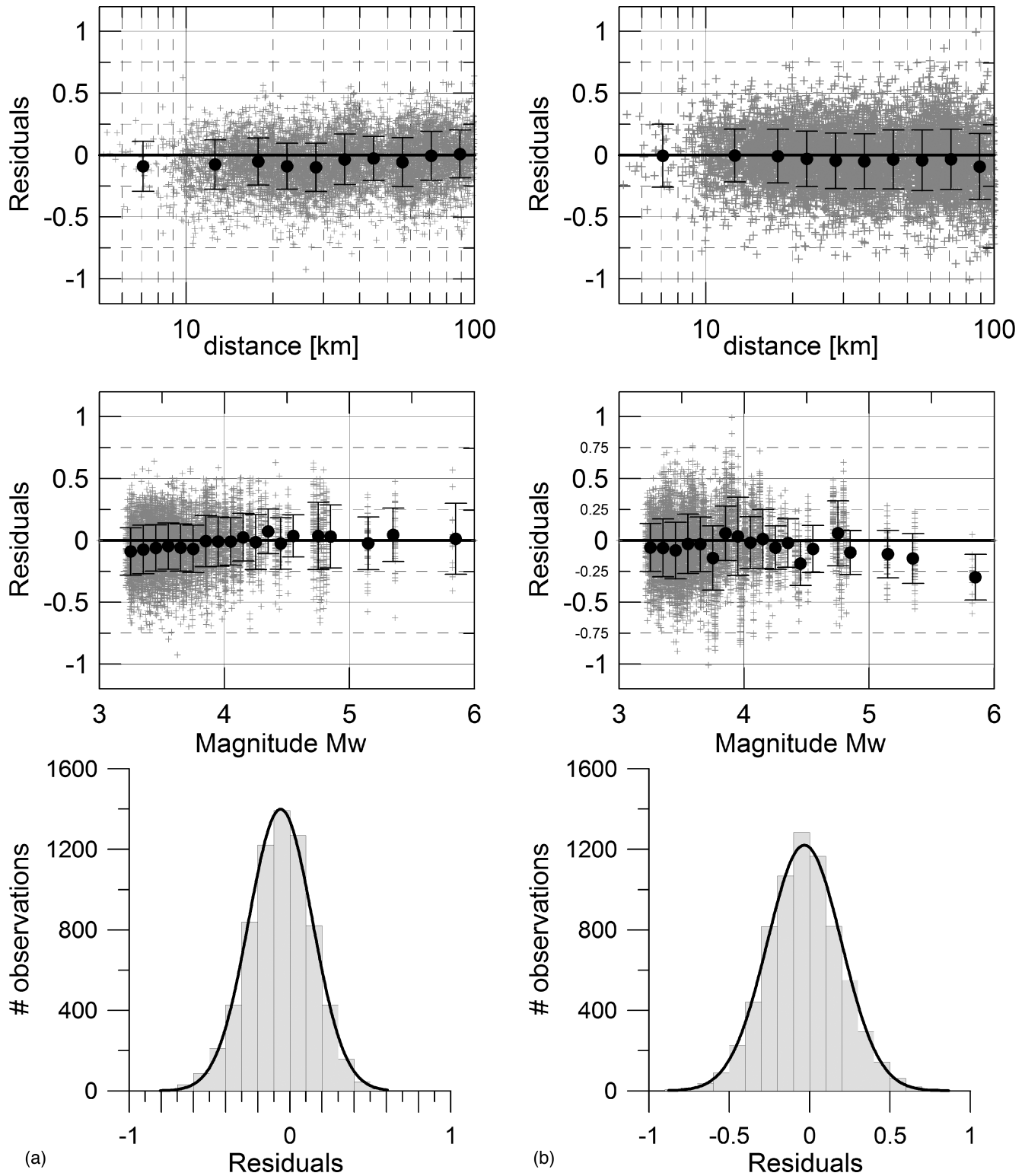


Figure 17. Residual distributions at 1 Hz (a) and 10 Hz (b), computed as \log_{10} (observed FAS/theoretical FAS). Top: residuals versus distance. Middle: residuals versus magnitude. Black circles and lines indicate mean residuals and standard deviations, for different distance and magnitude bins. Bottom: residual distributions and fitted normal distribution. Simulated values are computed, considering model B (eq. 11), where the stress drop is increasing with magnitude and depth (see the text for details).

This data set was selected after a validation procedure implying the removal of unreliable records and the evaluation of the SNR. All events were relocated and the local magnitude estimated adopting a specific velocity model for the region.

We applied a non-parametric generalized inversion to provide the complete set of spectral terms (e.g. attenuation, source parameters, source scaling and site effects) to predict ground motions in the area. Attenuation was parametrized by geometrical spreading as

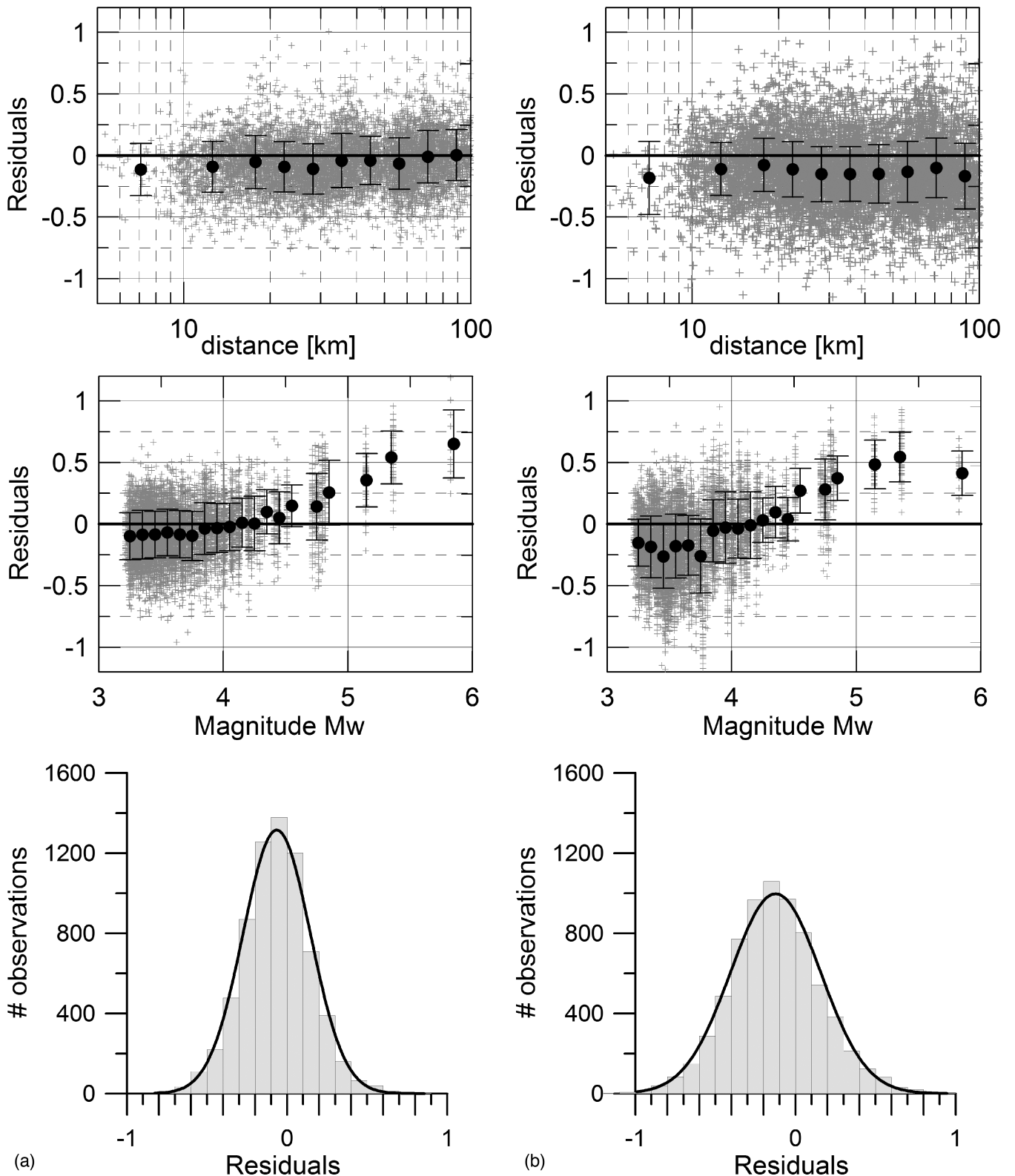


Figure 18. As Fig. 17, but considering a constant stress-drop value (2.6 MPa).

well as anelastic and scattering attenuation, while the source was interpreted using an omega-square model (Brune 1970) to estimate seismic moment and stress drop. The results were finally validated through a comparison with previous studies based on generalized inversion or other independent techniques (e.g. EGF).

The main results can be summarized as follows:

- Strong attenuation of S waves occurs at short and intermediate distances at all frequencies. We parametrize the empirical attenuations curves in terms of geometrical spreading, anelastic attenuation and high-frequency decay parameter k . The geometrical spreading

Table 6. Standard deviations at selected frequency of residual distributions.

Model	1 Hz	3 Hz	6 Hz	10 Hz	15 Hz	20 Hz
Variable stress drop	0.20	0.21	0.22	0.23	0.25	0.27
Constant stress drop	0.21	0.25	0.27	0.28	0.30	0.34

term is described by a piecewise linear model with crossover distances at 10 and 70 km (eq. 3 and Table 2). In the distance range 5–70 km the exponents of the geometrical spreading are greater than 1. Similar findings are also found in other worldwide regions and interpreted as a consequence of complex propagation effects in layered propagation medium. The associated quality factor $Q(f)$ and the high-frequency attenuation parameter k , are $Q(f) = 290f^{0.16}$ and $k = 0.012$ s, respectively, the latter being applied only for frequencies higher than 10 Hz. The proposed model is valid for a wide magnitude and distance range ($M_l = 3\text{--}5.8$ and $R = 5\text{--}120$ km).

(ii) The omega-square model adequately represents the source spectra and a quadratic scaling between M_w and M_l is proposed (eq. 9). When compared to the scaling obtained in previous studies for different regions, a regional dependence of the scaling is observed, being the curvature below magnitude 4.5 more pronounced for the two considered shallow crustal active regions (i.e. north-western Turkey and central Italy) than the curvature observed for stable and continental regions (central and northern Europe).

(iii) Stress drop variability within the 2009 L'Aquila sequence spans two orders of magnitude ($0.1 < \Delta\sigma < 25$ MPa) and is comparable with the range observed for seismic sequences in other Italian and worldwide regions. The average value is 2.6 MPa.

(iv) The stress drop can be described by a model that includes a dependence on seismic moment for magnitude larger than 3.75, and with an offset controlled by earthquake depth (eq. 11). The coefficients of the model are reported in Table 4.

(v) The site functions obtained by GIT inversion confirm the large variability of the site response in central Italy, with significant amplification over the entire frequency band. The vertical ground motions can be strongly amplified at low or high frequencies. The amplification of vertical ground motions explains the main discrepancies between the GIT site functions and H/V ratios.

The reliability of the parametric spectral models for attenuation $A(f, r)$ and source spectra $S(f)$ were tested simulating the observed acceleration spectra. To take into account the site effects, the corresponding empirical transfer functions were considered. The overall fit, evaluated through the residuals, indicates that the proposed source, site and attenuation models are suitable to describe the seismic motion recorded in the L'Aquila region.

ACKNOWLEDGEMENTS

This work was financially supported by ‘FIRB—Abruzzo’ Project (UR7) funded by Ministero dell’Istruzione dell’Università e della Ricerca (MIUR). We are grateful to the Associated Editor Y. Ben-Zion, Gail Atkinson and an anonymous reviewer for their useful comments that helped us to improve our work. We thank Giuliano Milana for encouraging us in this work and Chiara Felicetta for her help in preparing Figs 1 and 3.

REFERENCES

- Aki, K., 1967. Scaling law of seismic spectrum, *J. geophys. Res.*, **72**, 1217–1231.
- Allmann, B.P. & Shearer, P.M., 2007. Spatial and temporal stress drop variations in small earthquakes near Parkfield, California, *J. geophys. Res.*, **112**, B04305, doi:10.1029/2006JB004395.
- Ameri, G., Oth, A., Pilz, M., Bindi, D., Parolai, S., Luzi, L., Mucciarelli, M. & Cultrera, G., 2011. Separation of source and site effects by generalized inversion technique using the aftershock recordings of the 2009 L'Aquila earthquake, *Bull. Earthq. Eng.*, **9**(3), 717–739.
- Ameri, G., Gallovin, F. & Pacor, F., 2012. Complexity of the Mw 6.3 2009 L'Aquila (central Italy) earthquake: 2. Broadband strong motion modeling, *J. geophys. Res.*, **117**, B04308, doi:10.1029/2011JB008729.
- Anderson, J.G. & Hough, S.E., 1984. A model for the shape of the Fourier amplitude spectrum of acceleration at high frequencies. *Bull. seism. Soc. Am.*, **74**, 1969–1993.
- Andrews, D.J., 1986. Objective determination of source parameters and similarity of earthquakes of different size, in *Earthquake Source Mechanics*, pp. 259–267, eds Das, S., Boatwright, J. & Scholz, C.H., American Geophysical Union, Washington.
- Atkinson, G.M., 2004. Empirical attenuation of ground-motion spectral amplitudes in southeastern Canada and the northeastern United States, *Bull. seism. Soc. Am.*, **94**, 1079–1095.
- Atkinson, G.M., 2012. Evaluation of attenuation models for the northeastern United States/southeastern Canada, *Seismol. Res. Lett.*, **83**, 166–178.
- Babaie Mahani, A. & Atkinson, G.M., 2012. Evaluation of functional forms for the attenuation of small-to-moderate-earthquake response spectral amplitudes in North America, *Bull. seism. Soc. Am.*, **102**, 2714–2726.
- Bakun, W.H., 1984. Seismic moments, local magnitudes, and codaduration magnitudes for earthquakes in central California, *Bull. seism. Soc. Am.*, **74**, 439–458.
- Ben-Zion, Y. & Zhu, L., 2002. Potency-magnitude scaling relations for southern California earthquakes with $1.0 < \text{ML} < 7.0$, *Geophys. J. Int.*, **148**, F1–F5.
- Bergamaschi, F. et al., 2011. Evaluation of site effects in the Aterno river valley (Central Italy) from aftershocks of the 2009 L'Aquila earthquake, *Bull. Earthq. Eng.*, **9**, 697–715.
- Bianchi, I., Chiarabba, C. & Piana Agostinetti, N., 2010. Control of the 2009 L'Aquila earthquake, central Italy, by a high-velocity structure: A receiver function study, *J. geophys. Res.*, **115**, B12326, doi:10.1029/2009JB007087.
- Bindi, D., Castro, R., Franceschina, G., Luzi, L. & Pacor, F., 2004. The 1997–1998 Umbria-Marche sequence (central Italy): source, path, and site effects estimated from strong motion data recorded in the epicentral area, *J. geophys. Res.*, **109**, B04312, doi:10.1029/2003JB002857.
- Bindi, D., Pacor, F., Luzi, L., Massa, M. & Ameri, G., 2009. The Mw 6.3, 2009 L'Aquila earthquake: source, path and site effects from spectral analysis of strong motion data, *Geophys. J. Int.*, **179**, 1573–1579.
- Bindi, D., Luzi, L., Parolai, S., Di Giacomo, D. & Monachesi, G., 2011a. Site effects observed in alluvial basins: the case of Norcia (Central Italy), *Bull. Earthq. Eng.*, **9**(6), 1941–1959.
- Bindi, D., Pacor, F., Luzi, L., Puglia, R., Massa, M., Ameri, G. & Paolucci, R., 2011b. Ground motion prediction equations derived from the Italian strong motion database, *Bull. Earthq. Eng.*, **9**(6), 1899–1920.
- Boore, D.M., 1983. Stochastic simulation of high-frequency ground motion based on seismological models of the radiated spectra, *Bull. seism. Soc. Am.*, **73**, 1865–1894.
- Brune, J.N., 1970. Tectonic stress and the spectra of seismic shear waves from earthquakes, *J. geophys. Res.*, **75**, 4997–5009.
- Calderoni, G., Rovelli, A. & Singh, S.K., 2013. Stress drop and source scaling of the 2009 April L'Aquila earthquakes, *Geophys. J. Int.*, **192** (1), 260–274.
- Calderoni, G., Rovelli, A., Ben-Zion, Y. & Di Giovambattista, R., 2015. Along-strike rupture directivity of earthquakes of the 2009

- L'Aquila, central Italy, seismic sequence, *Geophys. J. Int.*, **203**(1), 399–415.
- Castro, R.R., Anderson, J.G. & Singh, S.K., 1990. Site response, attenuation and source spectra of *S* waves along the Guerrero, Mexico, subduction zone, *Bull. seism. Soc. Am.*, **80**, 1481–1503.
- Castro, R.R., Pacor, F., Puglia, R., Ameri, G., Letort, J., Massa, M. & Luzi, L., 2013. The 2012 May 20 and 29, Emilia earthquakes (Northern Italy) and the main aftershocks: *S*-wave attenuation, acceleration source functions and site effects, *Geophys. J. Int.*, **195**, 597–611.
- Chapman, M.C. & Godbee, R.W., 2012. Modeling geometrical spreading and the relative amplitudes of vertical and horizontal high frequency ground motions in eastern North America, *Bull. seism. Soc. Am.*, **102**, 1957–1975.
- ChiaraLuce, L., Valoroso, L., Piccinini, D., Di Stefano, R. & De Gori, P., 2011. The anatomy of the 2009 L'Aquila normal faults system (central Italy) imaged by high resolution foreshock and aftershock locations, *J. geophys. Res.*, **116**(B12), B12311, doi:10.1029/2011JB008352.
- Di Giulio, G., Gaudiosi, I., Cara, F., Milana, G. & Tallini, M., 2014. Shear-wave velocity profile and seismic input derived from ambient vibration array measurements: the case study of downtown L'Aquila, *Geophys. J. Int.*, **198**, 848–866.
- Drouet, S., Bouin, M.P. & Cotton, F., 2011. New moment magnitude scale, evidence of stress drop magnitude scaling and stochastic ground motion model for the French West Indies, *Geophys. J. Int.*, **187**, 1625–1644.
- Drouet, S., Chevrot, S., Cotton, F. & Souriau, A., 2008. Simultaneous inversion of source spectra, attenuation parameters, and site responses: application to the data of the French accelerometric network, *Bull. seism. Soc. Am.*, **98**, 198–219.
- Efron, B., 1979. Bootstrap methods: another look at the jackknife, *Ann. Stat.*, **7**(1), 1–26.
- Frankel, A., 1991. Mechanisms of seismic attenuation in the crust: scattering and anelasticity in New York State, South Africa, and southern California, *J. geophys. Res.*, **96**(B4), 6269–6289.
- Goertz-Allmann, B.P., Edwards, B., Bethmann Deichmann, N., Clinton, J., Fäh, D. & Giardini, D., 2011. A new empirical magnitude scaling relation for Switzerland, *Bull. seism. Soc. Am.*, **101**, 3088–3095.
- Grünthal, G., Wahlström, R. & Stromeyer, D., 2009. The unified catalogue of earthquakes in central, northern, and northwestern Europe (CENEC)—updated and expanded to the last millennium, *J. Seismol.*, **13**, 517–541.
- Hanks, T.C. & Kanamori, H., 1979. A moment-magnitude scale, *J. geophys. Res.*, **84**, 2348–2350.
- Hanks, T.C. & Boore, D.M., 1984. Moment-magnitude relations in theory and practice, *J. geophys. Res.*, **89**, 6229–6235.
- Herrmann, R.B., Malagnini, L. & Munafò, I., 2011. Regional moment tensors of the 2009 L'Aquila earthquake sequence, *Bull. seismol. Soc. Am.*, **101**, 975–993.
- Kanamori, H. & Rivera, L., 2004. Static and dynamic scaling relations for earthquakes and their implications for rupture speed and stress drop, *Bull. seism. Soc. Am.*, **94**, 314–319.
- Kawase, H., 2006. Site effects derived from spectral inversion method for K-NET, KiK-net, and JMA strong-motion network with special reference to soil non-linearity in high PGA records, *Bull. Earthq. Res. Inst. Univ. Tokyo*, **81**, 309–315.
- Konno, K. & Ohmachi, T., 1998. Ground-motion characteristics estimated from spectral ratio between horizontal and vertical components of microtremor, *Bull. seism. Soc. Am.*, **88**(1), 228–241.
- Lahr, J.C., 1989. HYPOELLIPSE—Version 2.0: a computer program for determining local earthquake hypocentral parameters, magnitude and first motion pattern, *Open-File Rep. U.S. Geol. Surv.*, **92**, 89–116.
- Luzi, L., Hailemikael, S., Bindi, D., Pacor, F., Mele, F. & Sabetta, F., 2008. ITACA (ITalian ACcelerometric Archive): a web portal for the dissemination of Italian strong-motion data, *Seismol. Res. Lett.*, **79**(5), 716–722.
- Malagnini, L., Mayeda, K., Nielsen, S., Yoo, S.H., Munafò, I., Rawles, C. & Boschi, E., 2014. Scaling transition in earthquake sources: a possible link between seismic and laboratory measurements, *Pure appl. Geophys.*, **171**(10), 2685–2707.
- Malagnini, L., Scognamiglio, L., Mercuri, A., Akinci, A. & Mayeda, K., 2008. Strong evidence for non-similar earthquake source scaling in central Italy, *Geophys. Res. Lett.*, **35**, L17303, doi:10.1029/2008GL034310.
- Malagnini, L., Akinci, A., Mayeda, K., Munafò, I., Herrmann, R. & Mercuri, A., 2011. Characterization of earthquake-induced ground motion from the L'Aquila seismic sequence of 2009, Italy, *Geophys. J. Int.*, **184**, 325–337.
- Margheriti, L. et al., 2011b. Rapid response seismic networks in Europe: lessons learnt from the L'Aquila earthquake emergency, *Ann. Geophys.*, **54**, (4), 392–399.
- Mayeda, K. & Malagnini, L., 2010. Source radiation invariant property of local and near-regional shear-wave coda: application to source scaling for the Mw 5.9 Wells, Nevada sequence, *Geophys. Res. Lett.*, **37**, L07306, doi:10.1029/2009GL042148.
- McNamara, D.E., Gee, L., Benz, H.M. & Chapman, M., 2014. Frequency-dependent seismic attenuation in the Eastern United States as observed from the 2011 Central Virginia earthquake and aftershock sequence, *Bull. seism. Soc. Am.*, **104**(1), doi:10.1785/0120130045.
- Mereu, R., Dineva, S. & Atkinson, G.M., 2013. The application of velocity spectral stacking to extract information on source and path effects for small-to-moderate earthquakes in southern Ontario with evidence for constant width faulting, *Seismol. Res. Lett.*, **84**, 899–916.
- Mitchell, B., 2010. Epilogue, *Pure appl. Geophys.*, **167**, 1581.
- Morozov, I., 2010. On the causes of frequency-dependent apparent seismological Q, *Pure appl. Geophys.*, **167**, 1131–1146.
- Oth, A., 2013. On the characteristics of earthquake stress release variations in Japan, *Earth planet. Sci. Lett.*, **377–378**, 132–141.
- Oth, A. & Kaiser, A.E., 2014. Stress release and source scaling of the 2010–2011 Canterbury, New Zealand, earthquake sequence from spectral inversion of ground motion data, *Pure appl. Geophys.*, **171**(10), 2767–2782.
- Oth, A., Bindi, D., Parolai, S. & Di Giacomo, D., 2011. Spectral analysis of K-NET and KiK-net data in Japan, Part II: On attenuation characteristics, source spectra, and site response of borehole and surface stations, *Bull. seism. Soc. Am.*, **101**(2), 667–687.
- Oth, A., Bindi, D., Parolai, S. & Wenzel, F., 2008. *S*-wave attenuation characteristics beneath the Vrancea region in Romania: new insights from the inversion of ground-motion spectra, *Bull. Seismol. Soc. Am.*, **98**, 2482–2497.
- Oth, A., Parolai, S., Bindi, D. & Wenzel, F., 2009. Source spectra and site response from *S* waves of intermediate-depth Vrancea, Romania, earthquakes, *Bull. seism. Soc. Am.*, **99**, 235–254.
- Oth, A., Bindi, D., Parolai, S. & Di Giacomo, D., 2010. Earthquake scaling characteristics and the scale-(in)dependence of seismic energy-to-moment ratio: insights from KiK-net data in Japan, *Geophys. Res. Lett.*, **37**, L19304, doi:10.1029/2010GL044572.
- Pacor, F. et al., 2011. Overview of the Italian strong motion database ITACA 1.0, *Bull. Earthq. Eng.*, **9**(6), 1723–1739.
- Paige, C.C. & Saunders, M.A., 1982. LSQR: an algorithm for sparse linear equations and sparse least squares, *ACM Trans. Math. Softw.*, **8**(1), 43–71.
- Paolucci, R., Pacor, F., Puglia, R., Ameri, G., Cauzzi, C. & Massa, M., 2011. Record processing in ITACA, the new Italian strong motion database, in *Earthquake Data in Engineering Seismology, Geotechnical, Geological and Earthquake Engineering Series*, Vol. 14, pp. 99–113, eds Akkar, S., Gulkan, P. & Van Eck, T., Springer, Berlin.
- Parolai, S., Bindi, D. & Augliera, P., 2000. Application of the generalized inversion technique (GIT) to a microzonation study: numerical simulations and comparison with different site-estimation techniques, *Bull. seism. Soc. Am.*, **90**, 286–297.
- Parolai, S., Bindi, D., Baumbach, M., Grosser, H., Milkereit, C., Karakisa, S. & Zünbüll, S., 2004. Comparison of different site response estimation techniques using aftershocks of 1999 Izmit earthquake, *Bull. seism. Soc. Am.*, **94**(3), 1096–1108.
- Parolai, S., Bindi, D., Durukal, E., Grosser, H. & Milkereit, C., 2007. Source parameters and seismic moment-magnitude scaling for Northwestern Turkey, *Bull. seism. Soc. Am.*, **97**, 655–660.
- Pinheiro, J.C. & Bates, D.M., 2000. *Mixed-effects Models in S and S-Plus*, Springer-Verlag.

- Pondrelli, S., Salimbeni, S., Morelli, A., Ekström, G., Olivieri, M. & Boschi, E., 2010. Seismic moment tensors of the April 2009, L'Aquila (Central Italy) earthquake sequence, *Geophys. J. Int.*, **180**, 238–242.
- Puglia, R., Ditommaso, R., Pacor, F., Mucciarelli, M., Luzi, L. & Bianca, M., 2011. Frequency variation in site response as observed from strong motion data of the L'Aquila (2009) seismic sequence, *Bull. Earthq. Eng.*, **9**, 869–892.
- Rovida, A., Camassi, R., Gasperini, P. & Stucchi, M. (eds), 2011. CPTI11, the 2011 Version of the Parametric Catalogue of Italian Earthquakes, Milano, Bologna. Available at: <http://emidius.mi.ingv.it/CPTI>, doi:10.6092/INGVIT-CPTI11.
- Salazar, W., Sardina, V. & de Cortina, J., 2007. A hybrid inversion technique for the evaluation of source, path, and site effects employing S-wave spectra for subduction and upper-crustal earthquakes in El Salvador, *Bull. seism. Soc. Am.*, **97**, 208–221.
- Scognamiglio, L., Tinti, E., Michelini, A., Dreger, D., Cirella, A., Cocco, M., Mazza, S. & Piattanesi, A., 2010. Fast determination of moment tensors and rupture history: application to the April 6th 2009, L'Aquila earthquake, *Seismol. Res. Lett.*, **8**, 892–906.
- Shearer, P.M., Prieto, G.A. & Hauksson, E., 2006. Comprehensive analysis of earthquake source spectra in southern California, *J. geophys. Res.*, **111**, B06303, doi:10.1029/2005JB003979.
- Tsuda, K., Koketsu, K., Hisada, Y. & Hayakawa, T., 2010. Inversion analysis of site responses in the Kanto Basin using data from a dense strong motion seismograph array, *Bull. seism. Soc. Am.*, **100**(3), 1276–1287.
- Tsuda, K., Archuleta, R.J. & Koketsu, K., 2006. Quantifying the spatial distribution of site response by use of the Yokohama high-density strong-motion network, *Bull. seism. Soc. Am.*, **96**, 926–942.
- Valoroso, L., Chiaraluce, L., Piccinini, D., Di Stefano, R., Schaff, D. & Waldhauser, F., 2013. Radiography of a normal fault system by 64,000 high-precision earthquake locations: The 2009 L'Aquila (central-Italy) case study, *J. geophys. Res.*, **118**(3), 1156–1176.
- Working Group SM-AQ, 2010. Microzonazione sismica per la ricostruzione dell'area aquilana. Regione Abruzzo - Dipartimento della Protezione Civile, L'Aquila, vol. 3. e DVD-rom. Available at: http://www.protezionecivile.gov.it/jcms/it/view_pub.wp?contentId=PUB25330, last accessed November 2015.
- Xie, J., 2010. Can we improve estimates of seismological Q using a new “Geometrical Spreading” model?, *Pure appl. Geophys.*, **167**, 1147–1162.
- Yenier, E. & Atkinson, G., 2015. Regionally adjustable generic ground-motion prediction equation based on equivalent point-source simulations: application to Central and Eastern North America, *Bull. seism. Soc. Am.*, **105**, 1989–2009.

SUPPORTING INFORMATION

Additional Supporting Information may be found in the online version of this paper:

Electronic supplement (<http://gji.oxfordjournals.org/lookup/suppl/doi:10.1093/gji/ggv448/DC1>).

Please note: Oxford University Press is not responsible for the content or functionality of any supporting materials supplied by the authors. Any queries (other than missing material) should be directed to the corresponding author for the paper.